Received 19 June 2022; revised 23 July 2022; accepted 26 July 2022. Date of publication 11 August 2022; date of current version 29 August 2022.

Digital Object Identifier 10.1109/OJAP.2022.3198269

A Cost-Effective Tethered-UAV-Based Coherent Near-Field Antenna Measurement System

RAIMUND A. M. MAUERMAYER [1] (Member, IEEE), AND JONAS KORNPROBST [2] (Graduate Student Member, IEEE)

[1] Independent Researcher, 71065 Sindelingen, Germany

[2] Chair of High-Frequency Engineering, Department of Electrical and Computer Engineering, Technical University of Munich, 80290 Munich, Germany

CORRESPONDING AUTHOR: R. A. M. MAUERMAYER (e-mail: raimund.mauermayer@ieee.org)

This article has supplementary downloadable material available at https://doi.org/10.1109/OJAP.2022.3198269, provided by the authors.

ABSTRACT For antenna measurements, the device under test (DUT) is usually transported to an anechoic chamber equipped with a scanner system. To measure on-site, unmanned aerial vehicles (UAVs) are a flexible solution as they can precisely maneuver a probe antenna over a surface in the DUT's near-field region. In this work, the designed multi-rotor UAV enables electromagnetically optimal placement of the probe antenna and effective gravity center re-balacing by payload position adjustment. The on-board software-defined radio (SDR) serves as a dual-channel receiver for the dual-polarized probe and as a signal source. For phase-coherent measurements, the source signal is transmitted to the DUT via an optical fiber tethering the UAV to the ground control station. Power supply cables allow unlimited flight times. A laser-based tracking system originating from virtual reality (VR) applications measures the probe position and orientation. The developed operator software guides the UAV along a trajectory and records the irregularly distributed near-field samples. An inverse equivalent sources solver (IESS) with full probe correction computes equivalent sources for antenna diagnostics and the DUT far field. The deployed components make the system very cost-effective. Still, verification measurements demonstrate its usability and the accuracy of the results for frequencies up to several GHz.

INDEX TERMS Near-field antenna measurement, unmanned aerial vehicle (UAV), software-defined radio (SDR), radio-frequency over fiber (RFoF), near-field to far-field transformation (NFFFT), inverse equivalent sources solver (IESS).

I. INTRODUCTION

FOR ALREADY more than a decade, there has been an unabated fascination for small unmanned aerial vehicles (UAVs) due to their precise maneuverability and the almost infinite range of possible applications. Meanwhile, drones are used for remote sensing and mapping in precision farming, visual inspection of infrastructure or industrial plants, or parcel delivery, to name just some of the most popular operation areas [1]. In April 2021, NASA's coaxial helicopter Ingenuity [2] accomplished its first autonomous exploration flight on the planet Mars.

The motivation to use UAVs in the field of antenna measurements mostly arises from the possibility to measure on site. This is of major interest when the environment of the antenna influences the radiated field as it might occur for broadcast [3], [4], aircraft navigation [5] or mobile communication [6] systems. On-site testing is also inevitable when the antenna is immobile or simply too large for any indoor measurement facility as is the case for the low-frequency antenna array (LOFAR) radio telescope [7], [8] and the square kilometer array (SKA) [9]. Small hovering platforms are also suitable for field distribution measurements due to their minimal scattering behavior compared to conventional probe positioning systems. This is beneficial, for example, for the quiet zone characterization of anechoic chambers [10]. Conventional mechanical multi-axis near-field scan systems typically perform measurements on simple canonical surfaces like a plane, cylinder, or sphere. Robotic arms offer more flexibility in the scan strategy [11], [12]. However, most of these systems have in common that they are stationary to ensure precise positioning of the probe antenna at predefined grid locations after alignment and

calibration of the axes. Furthermore, the range of the axes strictly limits the size of the scan area. To overcome the scan size limitations, the portable antenna measurement system (PAMS) [13] uses an overhead crane to move a gondola equipped with a probe antenna array around large satellite antennas. Acquiring the near-field measurements using a hand guided probe [14], [15] is probably one of the most flexible options to some extent, but impractical for electrically large antennas that require scan times of several hours and a uniform distribution of the field samples.

Fritzel *et al.* [16] were among the first to propose the usage of an unmanned aerial platform for near-field antenna measurement. The three main ingredients of such a system are the hovering platform itself that is maneuvered along a pre-defined trajectory, a 6-D tracking system to measure the position and orientation, also called pose, of the UAV and the installed probe antenna, and, of course, the radio-frequency (RF) equipment whose complexity depends on the possibly phaseless post-processing deployed.

Small multi-rotor UAVs — the first ingredient — became affordable and flexible platforms to carry a probe antenna. That is mainly a result of the development of low-cost inertial measurements units (IMUs) for flight stabilization based on microelectromechanical system (MEMS) accelerometer/gyroscope chips and fast power electronics for brushless motor controllers.

Accurate pose information from the tracking system — the second ingredient — is crucial for the exact transformation of near-field measurements to the far field. For direct far-field measurements, the position information is less important. In outdoor applications, the carrier phase evaluation of satellite signals in real-time kinematic (RTK) global navigation satellite systems (GNSSs) enables position accuracies of several centimeters and can provide attitude information with a multi-GNSS receiver configuration [17]. The position accuracy is sufficient for low frequencies [18], [19], [20], [21], [22], [23], [24], [25] and electrically small antennas up to a few GHz especially if magnitude only measurement data is used [26], [27], [28], [29]. Camera-based motion capture systems [30] as employed in [14], provide orientation and position information with sub-millimeter accuracy in a limited tracking volume using several active or passive infrared light reflecting markers attached to the UAV. Micrometer position accuracy is possible with the laser interferometry technique of laser trackers [31]. They determine the position of a spherically mounted reflector (SMR) by precise distance and angle measurements. Laser trackers were for example used in [16], [32], [33], [34], [35]. However, the complex optic and precise mechanics make them very expensive. Furthermore, the SMR's mirror must be aligned with the laser beam within a limited field of view angle. Thus, to avoid tracking losses due to UAV rotations, a complex gimbal mounting is required for the SMR. Even more sophisticated special active targets are necessary for laser-based attitude measurements [36]. Nonetheless, laser trackers achieve the range and accuracy needed for phase-coherent near-field measurements at several tens of GHz or electrically large-scale antennas such as satellite reflectors [13].

The RF equipment — the third ingredient — may comprise a simple power detector at a single polarized probe antenna on the UAV [26] if the post-processing does not require absolute phase information. Analogously, the UAV may serve as a flying test source [34], with a spectrum analyzer connected to the DUT on the ground. For phase-coherent measurements, the RF source and receiver need to be synchronized. Analog fiber optical connections are well suited to establish a phase-stable link for transmission measurements between the DUT on the ground and the UAV's probe antenna using a vector network analyzer (VNA) [35], [37]. The optical fiber tethers the UAV to the ground station, but hardly affects its maneuverability due to its low weight and mechanical flexibility compared to coaxial cables.

UAV-based near-field measurements also became feasible due to the development of near-field to far-field transformation (NFFFT) algorithms that can efficiently handle irregularly distributed sample points and correct for the influence of arbitrarily oriented probe antennas. The group of inverse equivalent source solvers (IESSs) [38], [39], [40], [41], [42], [43], [44], [45] which determine equivalent sources on a hull surface around the DUT to reconstruct the measured near-field samples, offers this flexibility. However, the evaluation of the underlying integral equations has to be accelerated, for instance, by the fast multipole method (FMM) or the multilevel FMM (MLFMM), to reduce the computational complexity. In this way, reasonable transformation times are achieved even for electrically large antennas [46], [47]. By appropriate modifications, inverse source solvers can also post-process magnitude-only near-field measurements. To reconstruct the phase information, near-field scans on multiple, spatially separated measurement surfaces [26] can be used. However, this does not guarantee to obtain the global optimum of the non-convex problem, i.e., the correct solution. For reliable phase reconstruction, multiple probes for partially coherent measurements seem to be necessary [48], [49] which can be challenging to mount on the UAV and increase receiver complexity.

The UAV-based measurement system presented in this contribution differs from the state-of-the-art found in publications that include concrete measurement results by the concept of a tethered UAV that allows phase-coherent near-field measurements and unlimited flight times.

In addition, the authors also had cost-effectiveness in focus when selecting the system components. Rather than using an off-the-shelf drone, a specialized UAV frame was designed that allows optimal payload placement and electromagnetically optimal placement of the probe antenna at the tip of the drone. The on-board dual-channel software-defined radio (SDR) serves as a RF source and receiver and simultaneously records the signals of the dual-polarized probe antenna. A power cable tethers the UAV to the ground to overcome the flight time limitation which would be imposed by batteries. Several optical fiber connections enable

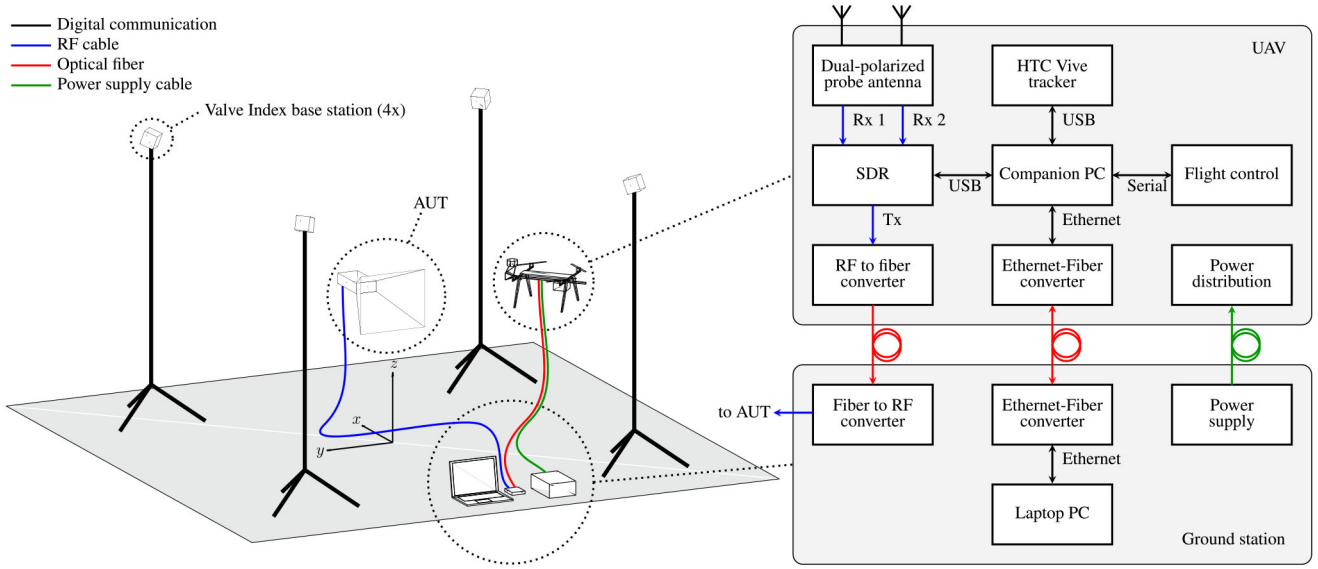

FIGURE 1. Overview of the complete UAV-based near-field antenna measurement system.

phase-coherent measurements and Ethernet communication. A consumer electronics tracking system, typically used for virtual reality (VR) applications, provides accurate position and orientation data to control the UAV along a planned path using a customized software that also records the pose and RF measurements. The fused measurements form the input for the fast irregular antenna field transformation algorithm (FIAFTA) [41], [43], [44] that transforms the irregular distributed near-field measurements to the far field. This work is a feasibility study demonstrating that the combination of the selected components and the custom acquisition software results in a well performing measurement system suitable for many (on-site) antenna measurement scenarios, e.g., mobile communication base station antenna measurements, provided that the local tracking system can be properly installed. Preliminary results from the initial version of the measurement system have already been given in [50], [51]. The experiences gained therein led to the evolved system in this work with improved RF and pose tracking performance.

Section II starts with an overview of the system architecture. Then, the UAV components and the RF equipment are described. The measurement data post-processing, including the FIAFTA, is briefly explained in Section III. Finally, validation results for a horn antenna are presented in Section IV.

II. UAV-BASED MEASUREMENT SYSTEM

A. MEASUREMENT SYSTEM CONCEPT

The overall architecture of the measurement system is shown in Fig. 1. Four Valve [52] Index lighthouse base stations on tripods are placed around the DUT. Together with the HTC Vive tracker [53] on the UAV, they form the 6-D tracking system. The UAV also carries the dual-polarized probe antenna connected to the on-board SDR receivers. The RF source signal, also generated by the SDR, is transmitted to the AUT over the RF over fiber (RFoF) link. Flight controller, tracker, and SDR are all connected to the companion PC that communicates with the ground station Laptop PC via a Ethernet over fiber link. A 24 V switching DC power unit on the ground supplies the tethered UAV with the required energy. If necessary, the power cables can also be replaced with extremely thin and lightweight wires using a high voltage switching-converter-based power transmission as proposed in [54]. The essential system components are described in more detail in the following.

B. UAV-BASED PROBE ANTENNA POSITIONING PLATFORM

1) MECHANICAL UAV FRAME DESIGN

Most commercially available multi-rotor UAV designs concentrate the payload in their center. That minimizes the moment of inertia and ensures good maneuverability. However, mounting the probe antenna close to the gravity center has the consequence that the drone frame and propellers affect the probe radiation pattern [55], [56], [57] and, thus, also the field measurement results as observed in [10]. To overcome this drawback of commercially available UAVs, a custom drone frame as shown in Fig. 2 was designed. It allows the placement of the probe antenna at the very front of the UAV. The aluminum frame consists of two parts: The upper section comprises the "H"-shaped propulsion system platform. The four brushless motors with 13 in propellers, the motor controllers, the flight controller, and the landing gear are rigidly installed to it. The lower section mainly consists of a center beam. The tracker-probe-antenna unit and the equipment carrier are attached to it. To balance the weight of the tracker-probe-antenna unit at the tip of the drone, the position of the equipment carrier for the companion PC, SDR and fiber-optic converters is adjustable along

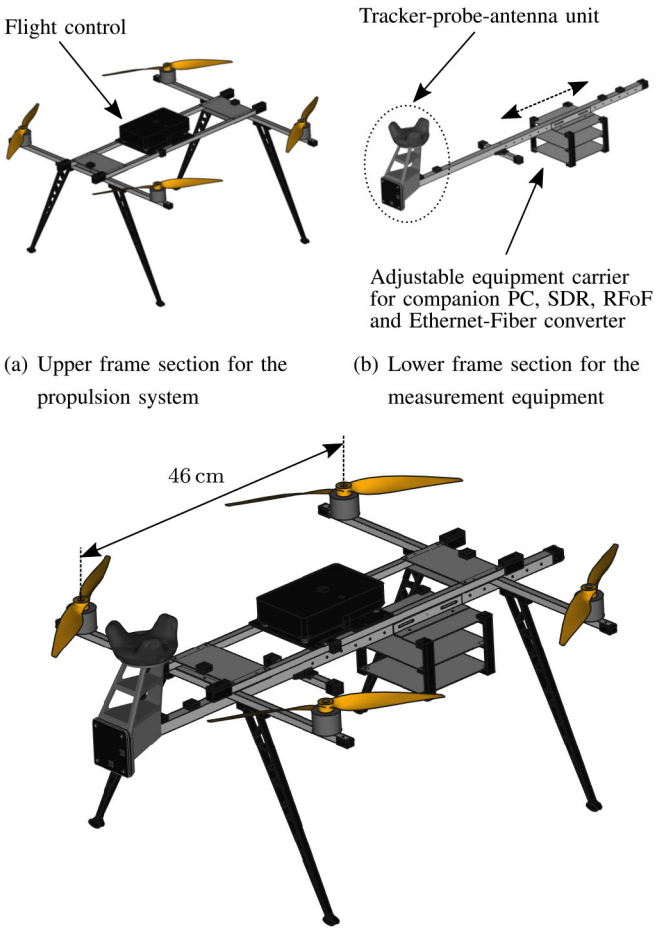

(a) Upper frame section for the propulsion system

(b) Lower frame section for the measurement equipment

(c) Assembled UAV frame

FIGURE 2. CAD drawings of the customized quadrotor UAV. The assembled frame in (c) consists of (a) the upper section for the propulsion system and (b) the lower section for the measurement equipment distributed on the tracker-probe-antenna unit and the slidable equipment carrier.

the center beam. Moreover, the lower section is mechanically decoupled from the upper section with elastic strings, which are not shown in the drawing, to keep propeller vibrations away from the measurement equipment. That is especially important for the IMU inside the HTC Vive tracker since the sensor fusion algorithm is tuned to track smooth movements of humans and, to the best of the authors' knowledge, cannot be tweaked to improve its robustness against vibrations. The power cable and the optical fibers from the ground station are connected to the gravity center of the UAV using a cardan joint to allow unobstructed rotations around all three UAV rotation axes for precise attitude control. Finally, all frame parts were painted in matte black to minimize reflections from the laser beams emitted by the lighthouse base stations, which would lead to tracking errors.

2) 6-D TRACKING SYSTEM

The tracking system is a core component of any near-field measurement system that is not based on precise mechanical positioners to move the probe antenna and/or the AUT

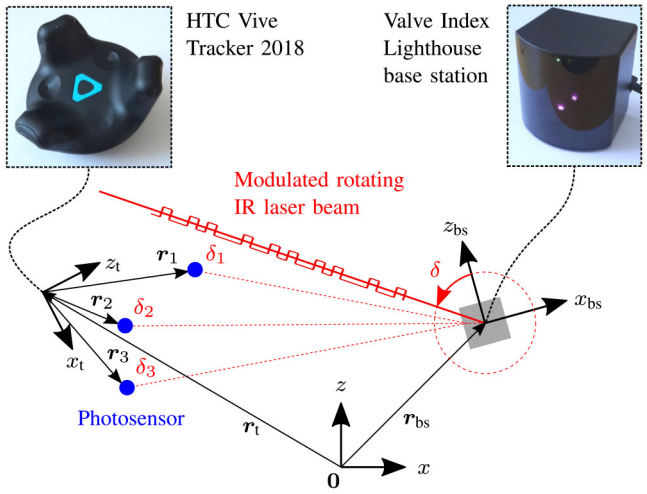

FIGURE 3. Operating principle of the tracking system illustrated for the 2-D case. The lighthouse base station emits a modulated rotating laser beam received by the photosensors of the tracker.

since the NFFFT requires accurate position and orientation information. The advent of VR applications led to the development of cost-effective methods to track players or objects in space. Therefore, the Valve Corporation [52] developed a 6-D tracking system with exceptional accuracy for less than $800 (including four base stations and one tracker). Due to its low cost, the tracking system has also already attracted attention in other research areas such as robotics [58], [59], [60], [61]. Camera-based systems are about ten times more expensive, and laser trackers have a even higher accuracy and range but are also up to a hundred times more expensive. In [50], the authors gained experience with the first generation of the system released in 2016, which only supported a maximum of two base stations. One of the base stations was shadowed by the DUT for certain near-field sample location leading to a reduced position accuracy. The second generation from 2019 overcomes this limitation and is used for this work with four base stations in combination with a HTC Vive Tracker 2018 [53] as sketched in Fig. 1.

The operating principle of the second generation of the tracking system is depicted in Fig. 3 for a simplified 2-D case. The lighthouse base station contains a rotating infrared (IR) fan beam laser, while the tracker is equipped with several infrared sensitive photosensors at well known locations $\boldsymbol{r}_{1,2,3}$ in the local tracker coordinate system (x_t, z_t). The modulated laser of the lighthouse transmits information about the current rotor angle δ, the orientation of the local base station coordinate system $(x_{\mathrm{bs}}, z_{bs})$ with respect to the gravity vector measured by an accelerometer, and base station calibration data [62]. The tracker receives this information whenever the rotating laser sweeps over the photosensors. Thus, the angles $\delta_{1,2,3}$ at which the sensors were hit by the laser are known. Based on the measured angles and the sensor positions $\boldsymbol{r}_{1,2,3}$, the location $\boldsymbol{r}_{\mathrm{bs}}$ and orientation of the base station in the tracker coordinate system can be estimated. In this manner, the pose of all base stations visible by the tracker

are determined during the system's calibration phase. After the calibration, the pose information of the stationary lighthouses, along with the measured angles, are the input for the non-linear pose estimator [63] to find the position and orientation of the tracker that best fits the measurements. The estimated tracker pose is fused with the tracker's IMU data to update the pose information during the revolution of the fan beam laser. For tracking in 3-D space, the lighthouse emits two orthogonal rotating laser fan beams. Although the unique determination of the 6-D pose requires a minimum of only four photosensors, the tracker is equipped with 23 photosensors to account for sensor occlusion and limited sensor sensitivity to shallow angles of incidence of the laser with respect to the sensor surface. With a range of 7 m specified for the lighthouse base station, mainly the tracking system limits the UAV's operating area. Up to 16 base stations can be distributed over the tracking volume. A combination of four tracking base stations can cover a volume of approximately up to $8 \times 8 \times 4$ m. However, staying below the maximum limits guarantees that all base stations are within the range of the tracker on the UAV improving the estimated pose accuracy.

Bauer *et al.* [64] comprehensively investigated the accuracy of the second generation Valve tracking system for static test setups. Regarding the system's precision, it was found that the standard deviation of the position is typically less than 0.5 mm if two lighthouse base stations are used. However, the system suffers from several systematic errors that limit the accuracy and strongly depend on the quality of the initial calibration. For example, a tilt of the horizontal reference plane of about 0.8° was observed which can easily lead to height errors of several centimeters depending on the size of the tracking area. Also, horizontal position errors were in the centimeter range, and tracker rotations around the origin of its local coordinate system map to position errors up to 10 mm. Hence, one can conclude that the overall accuracy of the system is rather in the centimeter range. This could be improved by more elaborated, but also more time-consuming, calibration routines that use multiple tracker locations to estimate the positions of the base stations. Nevertheless, the accuracy is assumed to be sufficient for near-field measurement up to several GHz.

3) FLIGHT CONTROL

The core task of the flight control is to stabilize the UAV in the air by adjusting the thrust of the motors based on the attitude estimation from its IMU. For this project, the well-established open-source flight control firmware PX4 autopilot [65] was chosen running on a Pixhawk 1 [66] hardware platform. The advantage of the PX4 firmware over other autopilots is the already built-in combined position and velocity controller that accepts position information from external tracking systems other than GNSS. The controller uses the pose information from the previously described tracking system to guide the UAV along a trajectory. Based on the flight dynamics of the UAV, the underlying proportional–integral–derivative (PID) position control loop was tuned carefully to find a compromise between a low position error, i.e., a small deviation of the actual drone position from the target position, and a too aggressive flight behavior.

4) COMPANION AND GROUND STATION PC

The small and lightweight single-board computer Raspberry Pi 3 [67] serves as a companion PC on the UAV. It is the hub for the communication between the on-board components and the ground station PC via the Ethernet over fiber link. The Raspberry Pi runs the proxy service MAVProxy [68] and communicates with the flight control over a serial, asynchronous connection. This allows configuration and remote control of the UAV from the ground station using the MAVLink [69] protocol. SDR and HTC Vive tracker are attached to the companion PC through the universal serial bus (USB). Both Linux PCs run the server-client application USB/IP [70], which enables interaction with the USB devices on the UAV as if they were directly attached to the local USB ports of the ground station PC. In this way, the tracking system's closed-source pose estimation software SteamVR [71] receives the raw angular data from the tracker over Ethernet instead of USB. It also simplified the development of the control software as available drivers for the SDR can be used without modification. In addition, a simple server application was implemented on the companion PC to control the RF signal routing switches of the calibration circuit that is introduced in Section II-C5.

5) CONTROL SOFTWARE

For convenient operation of the system, a control software with a graphical user interface (GUI) was developed using the cross-platform software development framework Qt [72]. A screenshot of the GUI running on the ground station PC during a measurement is shown in Fig. 4.

The application consists of four modules responsible for tracking system control, UAV operation, SDR configuration and measurement data recording, and the flight trajectory.

The pose information from the tracking system is accessed through the OpenVR [73] application interface and forwarded to the position estimator of the UAV. The position awareness of the drone enables autonomous flights and makes automatic take-off and land procedures possible. The operator does not have to care about manual maneuvering except for emergencies. The GUI allows basic configuration of the SDR, such as setting the measurement frequency, over the LimeSuite library [74]. On user request, the control software simultaneously records the pose data of the UAV from the tracking system and the complex samples from the two SDR receiver channels. As the devices are accessed asynchronously, the recorded data are time-stamped for subsequent alignment of the pose and RF information. The software uses a distance trigger to save measurements only when the drone has traveled a specified distance. This significantly reduces the number of redundant measurement points

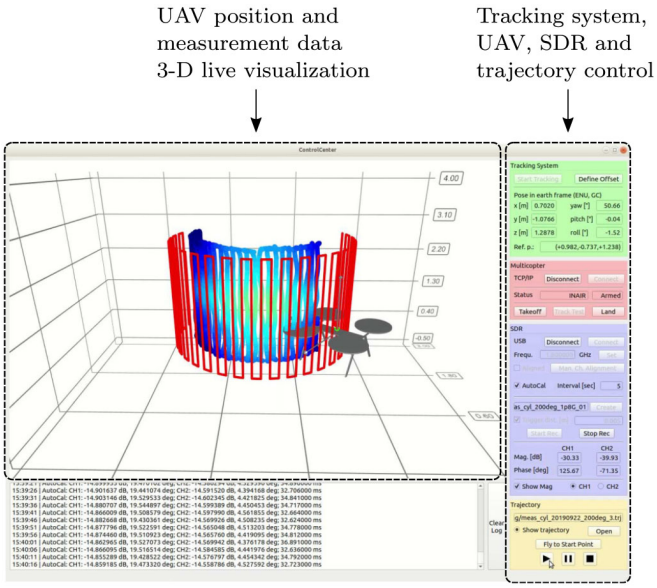

FIGURE 4. Customized GUI for measurement system control and measurement progress visualization. The planned trajectory is shown in red and the bluish color represents the measured near-field magnitude for a single probe port.

and ensures equidistant sampling during acceleration and deceleration phases. A predefined trajectory can be loaded into the software. When the user starts to stream the contained setpoints to the UAV's position controller, the drone follows the setpoints and is thus guided along the trajectory. To monitor the measurement process, the current UAV position, the trajectory, and the recorded near-field measurement data are displayed in a 3-D live visualization as exemplified in Fig. 4 for a running cylindrical scan.

6) TRAJECTORY PLANNING FOR NEAR-FIELD SCAN

Since the probe antenna is mounted at the drone's front without a tilt mechanism as used in [13], planar and cylindrical scan surfaces with the surface normal always pointing in horizontal direction are most suitable. The scan strategy must also consider that the power cable and optical fibers tether the UAV to the ground station. Therefore, vertical flight paths are preferred over horizontal trajectory sections to allow the cable to be pulled up from the ground and laid down neatly during ascent and descent flight phases. In this way, it does not have to be dragged sideways across the ground where it could get caught on obstacles. In such a case, the force exerted by the cable on the drone inevitable leads to large flight path deviations from the planned trajectory. Based on these considerations, the trajectory is composed of long vertical straight lines and short horizontal line or arc segments resulting in the vertical meandering path in Fig. 20(a). Often, the flight path is defined by only a few waypoints at turnpoints. With a typical cross-track navigation control approach, this can lead to large deviations of the actual flight path from the planned trajectory. As a consequence, the near field may not be sampled with the required density. In this

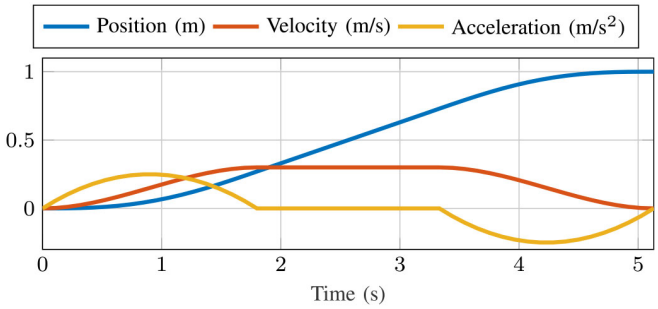

FIGURE 5. Position, velocity and acceleration profile of a typical trajectory segment with constraint maximum velocity and acceleration.

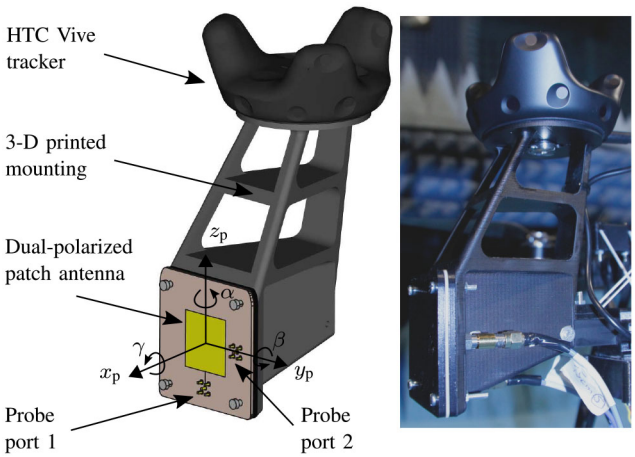

FIGURE 6. CAD drawing of the tracker-probe-antenna unit consisting of the HTC Vive tracker and a dual-polarized probe antenna on the left. The protective plastic cover of the patch antenna is removed for illustrative purposes. A photograph of the assembled unit is shown on the right.

work, the trajectory is formed by a time series of target positions/velocities and target yaw angles/rates. These setpoints are sent at intervals of 20 ms to the UAV's combined position and velocity controller which guides it exactly along the planned path. Due to the drone's dynamics characterized by its mass, inertia, and available thrust, the trajectory must meet side constraints on acceleration, velocity and angular rate. For a smooth flight, the acceleration should also be continuous to avoid sudden changes in commanded thrust. For that purpose, the target position is governed by forth order polynomials for acceleration and deceleration segments and first order polynomials for constant velocity phases. Fig. 5 shows a typical trajectory segment with acceleration and velocity restricted to 0.25 m/s^2 and 0.3 m/s, respectively. Flight path sections that are too short to reach the maximum target velocity at the given acceleration limit, such as the upper and lower meander edges in Fig. 20(a), are composed of fifth order polynomials.

C. RF MEASUREMENT SYSTEM

1) DUAL-POLARIZED PROBE-ANTENNA-TRACKER UNIT

For the head unit of the drone shown in Fig. 6, a 3-D printed, lightweight yet solid structure painted in matte black

was designed. It provides a mechanical interface to install various probe antennas. The HTC Vive Tracker is mounted on a pole to avoid narrowing the photosensors' field of view through occlusion. Still, it is placed as close as possible to the probe antenna to minimize position errors introduced by the transformation of the probe coordinate system into the tracker coordinate system caused by misalignment or errors of the estimated tracker orientation.

According to Huygens' principle [45], knowledge of the tangential electric and/or magnetic field components on the measurement surface is required to uniquely describe the field radiated by the AUT. Therefore, a dual-polarized probe antenna is employed. It allows simultaneous measurement of two almost orthogonal field polarizations using both SDR receiver channels. The probe antenna should have a rather smooth far-field pattern to minimize the impact of possible probe alignment or orientation measurement errors except for polarization angle errors. Moreover, a pattern with a wide beamwidth, i.e., a low directivity, is particularly suitable for planar and cylindrical measurements without a probe tilt mechanism to maximize the probe signal strength received from the AUT under large elevation angles. Finally, the antenna should exhibit a good front to back ratio in order to reduce the scattering influence of drone components behind the mounting structure. A dual-polarized patch is one of the simplest and most lightweight antenna that fulfills almost all the aforementioned requirements, except for a relatively high front to back ration to optimally minimize scattering of the UAV frame. Therefore, two patch antennas resonating at 1.8 GHz and 2.7 GHz were designed for the measurements presented in this contribution. Both were optimized with a protective 3-D printed plastic cover installed on top of the patch, as it can be seen in the photograph in Fig. 6 on the right. Since the accuracy of the tracking system is in the centimeter range using the manufacturer's calibration routine, only frequencies below 3 GHz were considered where the position error is certainly below one tenth of a wavelength. Moreover, the maximum frequency of the SDR is 3.8 GHz anyway. Regarding the rectangular horn that was used in the result Section IV as an AUT, one frequency was chosen below 2 GHz where the waveguide feed is excited with the fundamental mode to obtain a typical horn antenna far-field pattern. The other frequency was chosen above 2 GHz where the waveguide is already overmoded. In order to save weight, the companion PC and the Ethernet to fiber converter were installed in the equipment carrier without any metal housing. Thus, the frequencies 1.8 GHz and 2.7 GHz had to be selected where the electromagnetic interference was minimal. However, these emissions can of course be suppressed by proper shielding of the components.

For the probe correction inside the NFFFT, the probes' far fields of each port are required. They were measured in an anechoic chamber for the 2.7 GHz patch using the measurement setup shown in Fig. 7 and only simulated in CST Studio Suite [75] for the 1.8 GHz probe due to time constraints. Of course, it is generally recommended to measure the probe

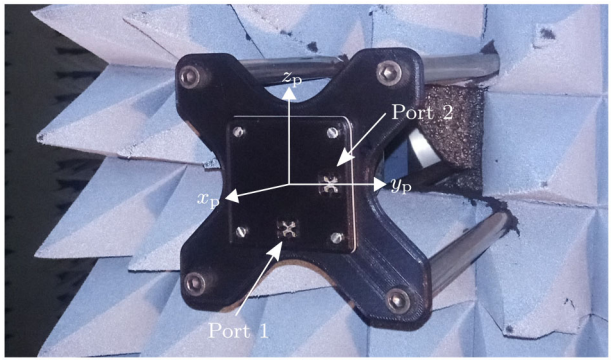

FIGURE 7. Dual-polarized probe patch antenna for 2.7 GHz installed to the roll-over-azimuth scanner with a 3-D printed mounting structure for the radiation pattern measurement.

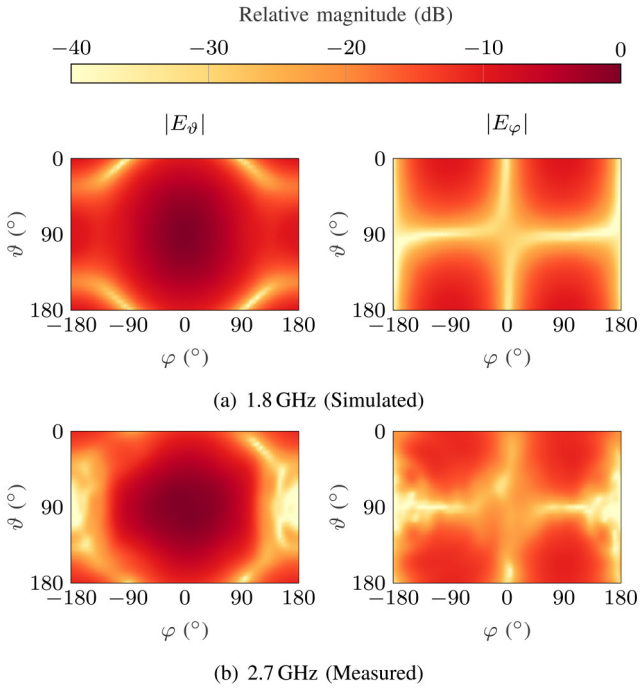

FIGURE 8. Normalized radiation patterns of the dual-polarized probe antennas for port 1. The pattern was (a) simulated for the 1.8 GHz probe and (b) measured for the 2.7 GHz probe.

antenna when it is installed on the UAV to improve the system's accuracy. However, mounting the complete UAV to the roll-over-azimuth positioner in a mechanically robust way is also not trivial. The normalized far field magnitude for port 1 of both dual-polarized patches is shown in Fig. 8(a) and Fig. 8(b). The radiation pattern for port 2 correspond to the one of port 1 rotated by 90° around the x_p-axis due to the symmetry of the antenna geometry.

2) UAV FRAME IMPACT ON PROBE ANTENNA PATTERN

Since the UAV frame design was particularly optimized for low interference with the probe pattern, this aspect was analyzed in detail by simulations for the 2.7 GHz probe patch antenna. Therefore, the UAV frame geometry in Fig. 2(c) was simplified for the simulation model shown in Fig. 9.

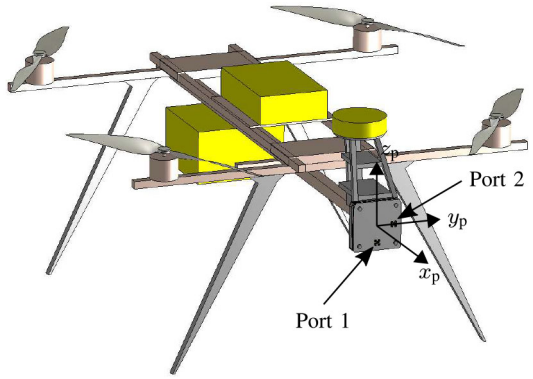

FIGURE 9. Simplified simulation model of the UAV frame in CST Studio Suite for the investigation of the influence of the frame components on the probe antenna radiation pattern.

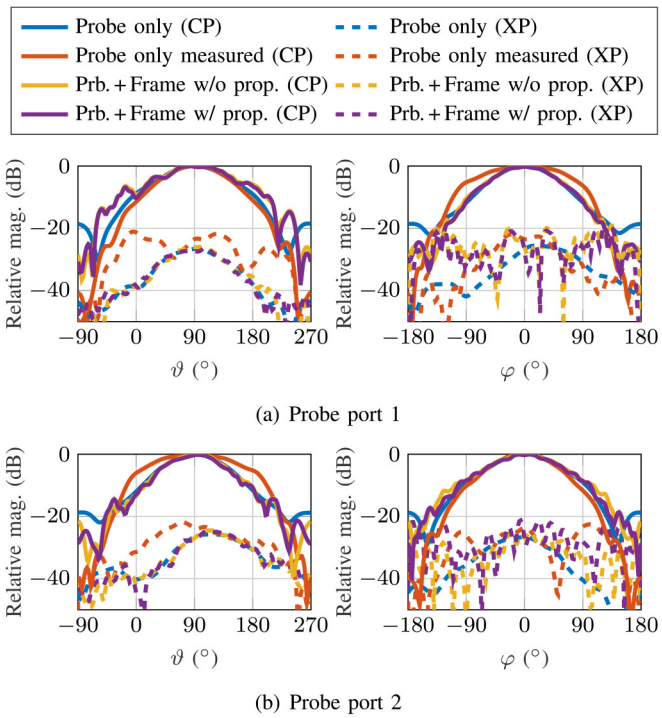

(a) Probe port 1

(b) Probe port 2

FIGURE 10. Simulated far-field results for the 2.7 GHz dual-polarized probe antenna with/without UAV frame and with/without propellers installed. For completeness, the measured radiation patterns of the isolated probe antenna are included. The co-polar/cross-polar field component is denoted by CP/XP.

The 3-D printed parts were modeled with a relative permittivity of 2.6 . The frame and all components containing electronics such as the tracker, the flight control and the equipment carrier were simplified as solid, highly conductive metal blocks. The carbon fiber propellers are also considered as metal objects to predict their worst case impact on the probe radiation pattern. Fig. 10 shows the simulated probe pattern cuts for both antenna ports and various configurations. For completeness, the measured patterns from Fig. 8(b) are included, showing that the fabricated patch antenna has a larger beamwidth in the H-plane than the simulation model. "Probe only" means that only the isolated probe antenna with the protective 3-D printed cover was considered. For "Prb. + Frame w/o prop.", the UAV frame was added in the simulation but the propellers were omitted. For "Prb. + Frame w/ prop.", also the propellers were included. From the simulations it can be concluded that the impact of the UAV frame on the probe pattern in the relevant angular range around the main beam is quite low for the co-polar (CP) field component. The cross-polar (XP) field component is more sensitive to the presence of the frame components especially in the horizontal cut. However, it is obvious that the frame design provides a stable radiation pattern that is certainly less affected by the UAV frame than it was observed in [56]. The probe pattern is primarily influenced by the closer probe mount and UAV frame parts. In comparison, the impact of the propellers is negligible. Propellers of a less conductive material certainly have an even smaller influence as demonstrated in [57] but typically do not provide the stiffness and light weight of carbon fiber propellers that are important for a fast thrust control response enabling accurate maneuverability. For broadband measurements, it is intended to use a probe with a higher front to back ratio, such as a 3-D printed quad-ridge antenna, which will help to further mitigate the UAV frame impact.

3) ON-BOARD SOFTWARE-DEFINED RADIO TRANSCEIVER

In wireless communication applications, RF signal processing is more and more shifted from the analog to the digital domain which allows to circumvent non-perfections of analog components and to implement new standards by simply updating the signal processing software. The flexibility of such software-defined radios (SDRs) drives the development of highly integrated transceiver ICs which, when receiving, condition, downmix the high-frequency signal and convert it to a digital complex baseband signal for further processing and vice versa when transmitting. For multiple-input multiple-output (MIMO) capability, they provide several parallel transmit and receive channels. These features plus their light weight and low cost make SDRs an attractive and versatile alternative to heavy and expensive VNAs. Their applicability in time domain antenna measurements has already been demonstrated in [76], [77].

Therefore, the LimeSDR[1] [78], available at a price of about $300, with a frequency range from 0.1 MHz to 3.8 GHz was installed in the equipment carrier of the UAV to simultaneously measure the two received RF signals from the dual-polarized probe antenna. A schematic of the RF components is shown in Fig. 14. The advantage of the LimeSDR over other commercially available SDRs is that the mixers of the transmit (Tx) and receive (Rx) stage can be fed by the same local oscillator (LO) [51]. This is essential for phase-coherent measurements, since the SDR's transmitter is used to excite the DUT with a continuous wave (CW)

1. In June 2022, the end of production was announced for the LimeSDR due to semiconductor shortcomings.

signal at the desired measurement frequency f. When operating the transmitter and receiver at the same frequency, it was observed that significant internal crosstalk between the RF paths occurs which is mainly attributable to the SDR's compact design. Through additional shielding on the SDR's printed circuit board (PCB) it was possible to reduce the crosstalk to about -60 dB. In addition, the external 30 dB amplifier AMP 1 raises the Tx signal level. This helps to lower the SDR's Tx power to such a level that the crosstalk signal is in the range of the resolution limit of the 12-bit analog to digital converters (ADCs).

A well known drawback of direct conversion receivers is that, for example, internal LO leakage leads to a DC offset at the receiver mixer output that reduces the ADC's dynamic range. Hence, the offset is permanently corrected by a compensation loop [79]. Measurements exactly at the LO frequency are consequently not possible because the received signal would be canceled by the DC offset correction. Therefore, the SDR's numerically controlled oscillator (NCO) is used to shift the constant Tx base band signal by 2 MHz before it is mixed with the LO at $f - 2$ MHz to generate the RF signal for the AUT. The received RF signals are first mixed to an intermediate frequency (IF) of 2 MHz using the Tx LO for phase-coherence. Only in the digital domain the base band signals are down-converted to zero IF by another NCO. In this manner, the narrow-band measurement signal is not affected by the mixers' DC offset compensation. Moreover, no further transform from time to frequency domain is required to obtain the complex signal at the measurement frequency. The received IF signal is sampled at a rate of 10 MHz. After down-conversion to zero IF, the SDR's decimation filter reduces the sampling rate by a factor of 32 so that complex samples are sent to the ground station at a rate of 312.5 kHz for both channels. Finally, an averaging filter with length 340 is applied to achieve a measurement sample interval of about 1 ms. This is more than sufficient to fulfill the spatial near-field sampling requirement for the intended electrical DUT sizes and UAV flight speeds.

4) RF OVER FIBER CONNECTION

The coherent field measurement requires a phase-stable transmission of the Tx signal from the SDR on the UAV to the DUT on the ground. Coaxial cables are considered unsuitable for this application, not only because of their weight and stiffness, but also due to the high cost of low-loss and phase-stable cables. In contrast, fiber optical cables are lightweight (less than 1 g/m for a 0.9 mm diameter fiber), flexible, phase-stable, have negligible losses and they are very cost-effective as they are mass products in digital network communication. However, converters are needed for the transition from conductive to optical transmission. Commercially available converters are rather expensive, bulky and often too complex for the simple transmission of the CW signal with constant power in this work. Therefore, the miniature RFoF link shown in Fig. 11 was designed from components for a total of less than $200.

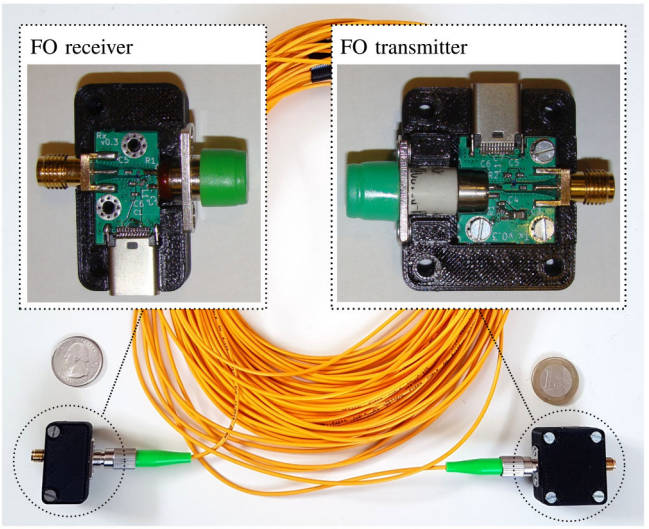

FIGURE 11. Miniature RFoF link for the transmission of the SDR Tx signal from the UAV to the AUT.

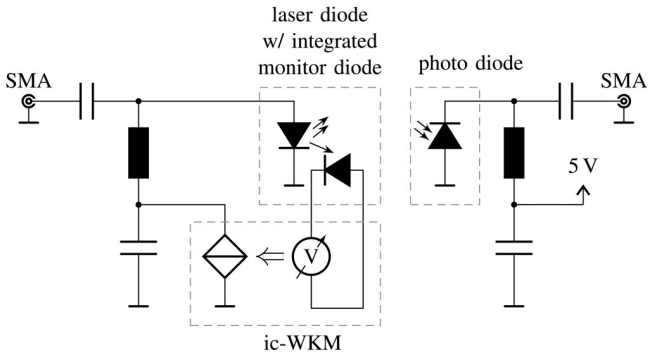

(a) FO transmitter: amplitude-modulated laser diode with quiescent point stabilization

(b) FO receiver: photo-diode-based detector

FIGURE 12. Simplified schematics of (a) the FO transmitter and (b) the FO receiver.

The RF architecture with a transmitting AUT and the SDR on board the UAV offers several advantages with regard to the tethered RF connection. First, only one RF connection between the UAV and the ground station is necessary instead of multiple connections for a multi-channel receiver on the ground as proposed in [37]. Second, a drift correction as suggested in the following Section II-C5 can be implemented directly on the UAV without additional RF loop-back paths from a receiver on the ground to the pre-amplifiers on the UAV required to compensate the RFoF link losses. Third, the signal transmitted over the RFoF connection is a constant CW signal. Hence, non-linearities on the RF path to the radiating AUT, e.g., caused by the diodes or amplifiers, have no influence on the measured probe antenna signal.

As shown by the simplified circuit diagram in Fig. 12(a), the fiber optical (FO) transmitter is built from a 1310 nm laser diode [80] whose output signal is amplitude-modulated

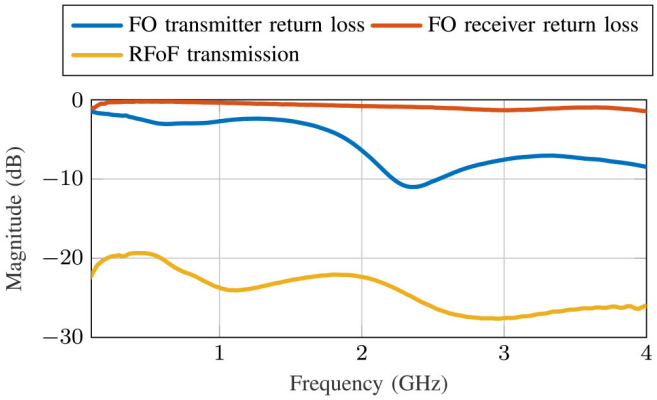

FIGURE 13. S-parameter measurement results for the RFoF link.

by the SDR Tx signal. The laser diode driver ic-WKM [81] controls the diode bias current based on the feedback of a laser diode integrated monitor photo diode such that the optical output power is stabilized against temperature or supply voltage variations. The control bandwidth of this feedback loop is orders of magnitude lower than the frequencies of the modulating RF signal. Due to the low differential resistance of the laser diode at the quiescent point, the FO transmitter has a small input return loss. A series resistor between the bias tee and the laser diode could be inserted to improve matching. However, this would reduce the signal conversion efficiency and, hence, it was omitted since AMP 1 can drive the low impedance at its output. As shown in Fig. 12(b), the FO receiver only consists of a reverse-biased photo diode using a lumped element bias tee. The laser diode has to be equipped with an optical isolator that guarantees a high return loss in order to avoid multiple reflections between the laser and photo diode. These reflections would cause optical interference at the photo diode interface, translating to magnitude changes of the received RF signal. Due to the small optical wavelength, even slight variations in the optical propagation on the fiber caused by flexing or temperature changes would have a significant impact on the RF signal transmission.

The PCBs of the converters are housed in 3D-printed cases and power is conveniently supplied via USB-C connectors. As the optical converters are used in the Tx path with high signal power levels, their noise figure is not critical for the application. The measured S-parameters in Fig. 13 show that the optical link has a conversion loss of 20–30 dB which is compensated by amplifier AMP 2 in Fig. 14.

5) CALIBRATION CIRCUIT

The usage of a dual-polarized probe antenna requires careful receiver channel balancing in terms of magnitude and phase for the subsequent NFFFT. First test flights revealed magnitude drifts over the measurement time caused by temperature changes of the RF equipment on the UAV. To overcome these issues, a calibration circuit with the schematic in Fig. 14 was implemented from four single-port-double-throw (SP2T)

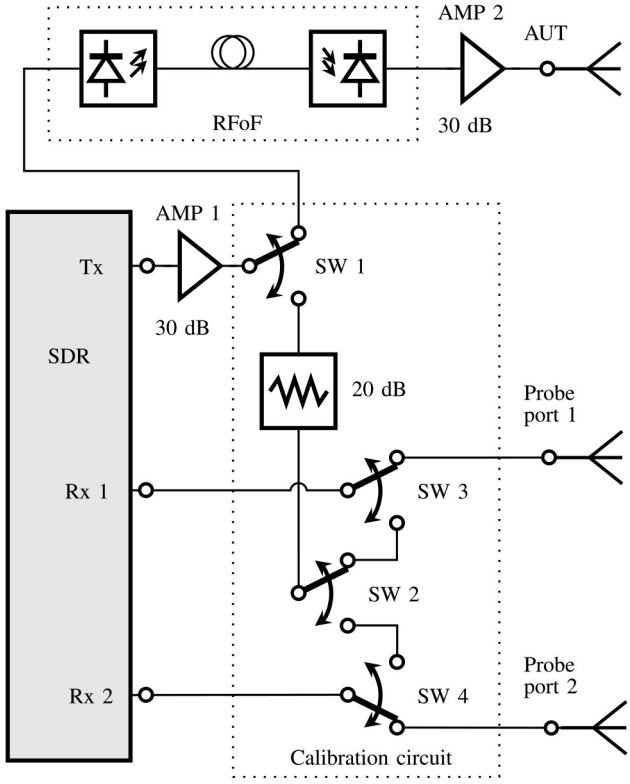

FIGURE 14. Schematic of the RF components including the calibration circuit for channel alignment and temperature drift compensation.

non-reflective RF switches [82]. During the near-field measurement, the switches SW 3/4 connect the two SDR Rx channels to the ports of the dual-polarized probe antenna and the switch SW 1 routes the SDR Tx signal to the DUT. For the through calibration measurements, the switch SW 1 is toggled and routes the SDR Tx signal consecutively to the SDR Rx 1/2 inputs via the switches SW 2 and SW 3/4. The 20 dB attenuator prevents receiver overloading and in combination with the RF switches, the total loopback attenuation from the Tx to Rx port of the SDR approximately corresponds to the minimum path loss between the AUT and the probe antenna. Thus, Tx and Rx gains can be kept the same during the calibration and measurement phase.

When the system is turned on, especially the SDR starts to heat up as it consumes several Watts of power and is cooled only by air convection. After take-off, the propeller downwash generates a cooling airflow around the equipment carrier and the thermal equilibrium of the RF equipment settles at a lower temperature. To correct the thermal drift of the measured signals, the calibration is performed every 5 s throughout the measurement. Fig. 15 shows the magnitude and phase of these through-calibration measurements at 2.7 GHz for about 10 min after takeoff. The through measurements are related to their initial value to evaluate the drift behavior. The signal magnitudes slightly increase for both channels until thermal equilibrium is reached after about

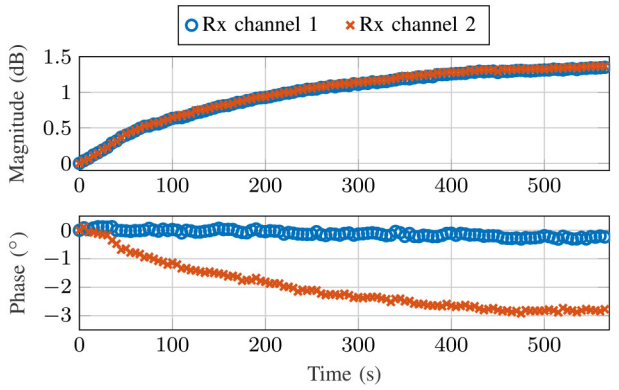

FIGURE 15. Through calibration measurements for both SDR Rx channels 1 and 2 at 2.7 GHz for a time span of about 10 min after UAV takeoff. The measurements are related to their initial value.

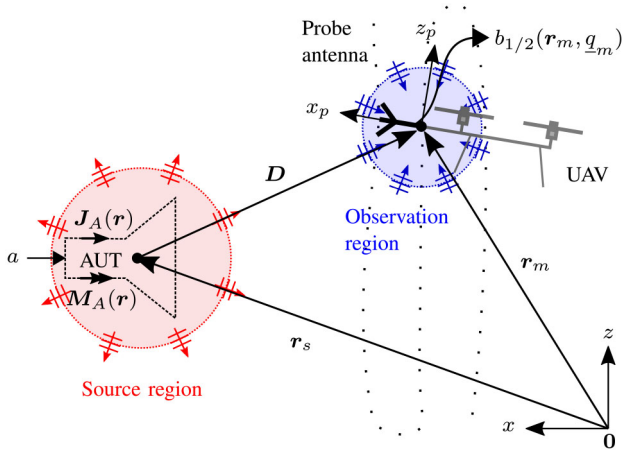

FIGURE 16. Definition of the equivalent surface current densities on the AUT hull surface in the global coordinate system. $b_{1/2}(\boldsymbol{r}_m, \underline{q}_m)$ is the signal at the probe antenna port 1/2 for the excitation a of the AUT.

400 s. With a drift of less than 3°, the phase proved to be rather robust against temperature changes.

III. MEASUREMENT DATA POST-PROCESSING

A. POSE AND RF DATA ALIGNMENT

As the pose and RF signals are sampled asynchronously, the data streams need to be merged according to their timestamps. Accurate spatial interpolation of the complex RF samples using a local interpolation scheme generally requires a high oversampling factor and is not recommended. Therefore, instead of the RF signal, the probe location and orientation are linearly interpolated at the RF sample time, assuming a constant velocity translation and rotation between two pose measurements. Interpolation of the probe position at the time of the RF sample is straightforward. The probe orientation angles require more caution. The Euler angles α, β and γ, as indicated in Fig. 6, are not well suited for interpolation. They are also unable to uniquely describe the orientation without a convention for the sequence of rotations around the coordinate system axes. For these reasons, the probe orientation is described by the unit quaternion

$$\underline{q} = \left(\cos\frac{\zeta}{2}, \hat{a}\sin\frac{\zeta}{2}\right) \tag{1}$$

that overcomes the disadvantages of Euler angles. It uniquely represents the rotation by the 3-D rotation axis unit vector $\hat{a}$ and the rotation angle ζ. With the spherical linear interpolation (SLERP) [83] for quaternions, the orientation of the probe antenna is calculated at the RF sample time. Prior to the NFFFT, the calibration data, recorded during the flight using the previously described calibration circuit, is applied to the RF samples to balance the receiver channels and to correct the temperature drift.

B. FIELD TRANSFORMATION ALGORITHM

Since the drone does not exactly follow the predefined trajectory, the measurement points are irregularly distributed, and also the probe orientation can vary arbitrarily. Thus, a field transformation that efficiently processes near-field data of this kind is vital for the measurement system. For the presented system, the fast irregular antenna field transformation algorithm (FIAFTA) is employed, which is based on the propagating plane-wave-based near-field transmission equation [42]

$$b_{1/2}\left(\boldsymbol{r}_m, \underline{q}_m\right) = \frac{aF}{-2\mathrm{j}k} \lim_{L\to\infty} \oiint \overline{\boldsymbol{R}}\left(\underline{q}_m\right) \cdot \boldsymbol{W}_{1/2}^{\mathrm{Probe}}\left(-\overline{\boldsymbol{R}}\left(\underline{q}_m\right)^{\mathrm{T}} \cdot \hat{k}\right) \cdot \boldsymbol{W}^{\mathrm{AUT}}\left(\hat{k}\right) T_L\left(kD, \hat{k}\cdot\hat{D}\right) \mathrm{d}^2\hat{k}. \tag{2}$$

As illustrated in Fig. 16, (2) describes the probe signal $b_{1/2}(\boldsymbol{r}_m, \underline{q}_m)$ at port 1/2 for the position $\boldsymbol{r}_m$ and the orientation quaternion $\underline{q}_m$ at the m-th measurement point. The AUT is excited by the signal a. $\boldsymbol{W}_{1/2}^{\mathrm{Probe}}(\hat{k})$ is the gain normalized far field for probe port 1/2 in the local probe antenna coordinate system. The gain normalized AUT far field

$$\boldsymbol{W}^{\mathrm{AUT}}\left(\hat{k}\right) = \frac{-\mathrm{j}k}{\sqrt{4\pi}a} \oiint_A \left[\left(\bar{\boldsymbol{I}} - \hat{k}\hat{k}\right)\cdot\boldsymbol{J}_A(\boldsymbol{r}') - \frac{1}{Z_0}\hat{k}\times\boldsymbol{M}_A(\boldsymbol{r}')\right] \mathrm{e}^{\mathrm{j}k\hat{k}\cdot(\boldsymbol{r}'-\boldsymbol{r}_s)}\,\mathrm{d}A' \tag{3}$$

is given with respect to the source region center $\boldsymbol{r}_s$ and depends on the equivalent electric and magnetic surface current densities $\boldsymbol{J}_A(\boldsymbol{r}')$ and $\boldsymbol{M}_A(\boldsymbol{r}')$ on the enclosing AUT hull. The term "gain normalized" implies that $|W_{\vartheta/\varphi}| = \sqrt{G_{\vartheta/\varphi}}$, i.e., the magnitude of spherical far-field component $W_{\vartheta/\varphi}$ corresponds to the square root of the realized antenna far-field gain $G_{\vartheta/\varphi}$. $\bar{\boldsymbol{I}}$ is the unit dyad and $\boldsymbol{k} = k\hat{k}$ the wave vector pointing in radial direction $\hat{k}$, where the hat $\hat{}$ indicates a unit vector. Z_0 is the characteristic impedance of the background medium which is typically assumed to be vacuum. The rotation dyad $\overline{\boldsymbol{R}}(\underline{q}_m)$ considers the orientation of the probe antenna in the global coordinate system. The

translation operator $T_L(kD, \hat{k} \cdot \hat{D})$, which is known from the FMM [84], relates the outgoing plane-wave spectrum of the AUT sources to an incoming plane-wave spectrum with respect to the probe location $\boldsymbol{r}_m$. The incoming plane waves are weighted with the far field of the probe antenna. Direct use of the probe antenna's far field for full probe correction [85] is a positive side effect of the propagating plane-wave-based field translation. Source and observation region in Fig. 16 are separated by the translation vector $\boldsymbol{D} = D\hat{D} = \boldsymbol{r}_m - \boldsymbol{r}_s$. In practice, the underlying multipole expansion is truncated at a certain order L according to the sum of the source and observation region radii and the desired operator accuracy. Integration of the incoming plane-wave spectrum over the unit sphere results in the received probe signal. The complex factor F in (2) takes impedance mismatches, cable attenuation and other RF system losses or gains into account.

The equivalent surface current densities

$$\boldsymbol{J}_A(\boldsymbol{r}') = \sum_p J_p \boldsymbol{\beta}_p(\boldsymbol{r}'), \quad \boldsymbol{M}_A(\boldsymbol{r}') = \sum_q M_q \boldsymbol{\beta}_q(\boldsymbol{r}') \tag{4}$$

are discretized using Rao-Wilton-Glisson (RWG) [86] basis functions $\boldsymbol{\beta}_{p/q}(\boldsymbol{r})$ on the triangular mesh of the AUT hull surface. Discretization of (2) leads to the equation system

$$\boldsymbol{A}\boldsymbol{x} = \boldsymbol{b}, \tag{5}$$

where the coupling matrix $\boldsymbol{A}$ represents the interaction between each RWG basis function and the probe antenna at all measurement locations. $\boldsymbol{b}$ contains the RF measurement samples $b_{1/2}(\boldsymbol{r}_m, \underline{q}_m)$ and $\boldsymbol{x}$ the unknown basis function coefficients J_p and M_q. To solve the typically under-determined equation system, the normal error (NE) equation [87], [88]

$$\boldsymbol{A}\boldsymbol{A}^{\mathrm{H}}\boldsymbol{y} = \boldsymbol{b} \tag{6}$$

with

$$\boldsymbol{x} = \boldsymbol{A}^{\mathrm{H}}\boldsymbol{y} \tag{7}$$

is formulated. The superscript $^{\mathrm{H}}$ denotes the conjugate transpose, i.e., the Hermitian, of the matrix. In combination with an iterative solver such as the generalized minimal residual (GMRES) [87] solver, the NE equation has the advantage that the relative solver residual $\|\boldsymbol{A}\boldsymbol{A}^{\mathrm{H}}\boldsymbol{y} - \boldsymbol{b}\| / \|\boldsymbol{b}\|$ directly indicates how well the equivalent sources of the current iteration reconstruct the measurements. The iterative solver is stopped when a certain error criteria is reached or when the residual starts to stagnate in order to exploit regularization properties of the GMRES solver for the ill-posed inverse problem.

Since (5) does not impose any constraint on the field interior to the AUT hull, the solution for the electric and magnetic currents is ambiguous, i.e., the surface currents do not necessarily resemble the actual near field of the AUT on the hull. Thus, to obtain a unique solution that is also suitable for diagnostic applications, the so-called Love currents [45] are computed in a post-processing step applying a Calderón projection operator [89] to the surface currents. It enforces the interior zero field condition without changing the exterior field. Once the equivalent sources are determined, the AUT's far field is computed from them using (3).

To speed up the evaluation of (2) for the computation of the matrix vector products in (6), the regions containing the sources and measurement points are subdivided into boxes and organized in an octree. This allows a hierarchical matrix vector product evaluation that reduces the number of explicitly computed interactions between source and observation regions similar to the MLFMM [84]. For more details about the FIAFTA, the reader is referred to [41], [45].

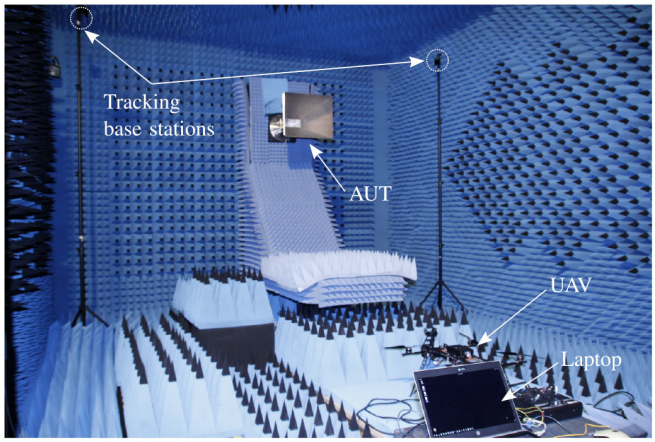

FIGURE 17. Photograph of the measurement setup in the anechoic chamber at the Technical University of Munich. Two of the four tracking base stations are located on tripods behind the photographer and are therefore not visible.

IV. MEASUREMENT RESULTS

A. MEASUREMENT SETUP IN ANECHOIC CHAMBER

The measurement system was set up in the anechoic chamber at the Technical University of Munich as the photograph in Fig. 17 shows. Two of the four tracking base stations sketched Fig. 1 are located on tripods behind the photographer and are therefore not visible. The AUT is mounted to the roll-over-azimuth positioner of the chamber. In this way, a standard spherical near-field (SNF) scan and the UAV measurements can be performed in the same well-controlled environment allowing good comparability of the results. The far-field from the SNF scan is considered as a reference. Thereby, it has to be taken into regard that scattering, e.g., from the roll-over-azimuth positioner, affects the UAV-based and SNF results differently. This is because spatial filtering is more effective when the probe antenna is moved around the AUT than when the (stationary) probe is at a fixed location and the AUT is rotated. Fig. 18 shows the horn antenna used as an AUT in more detail. Since measurements are performed at 1.8 GHz and 2.7 GHz, the Fraunhofer far-field distance is 4.9 m and 7.4 m according to the horn's aperture size of 0.49 m × 0.41 m. The center of the aperture is approximately at (2.13 m, 0.05 m, 1.82 m) in the tracking system coordinate system. The assembled quad-rotor UAV platform is shown in Fig. 19. The presented measurements were obtained on a cylindrical scan surface.

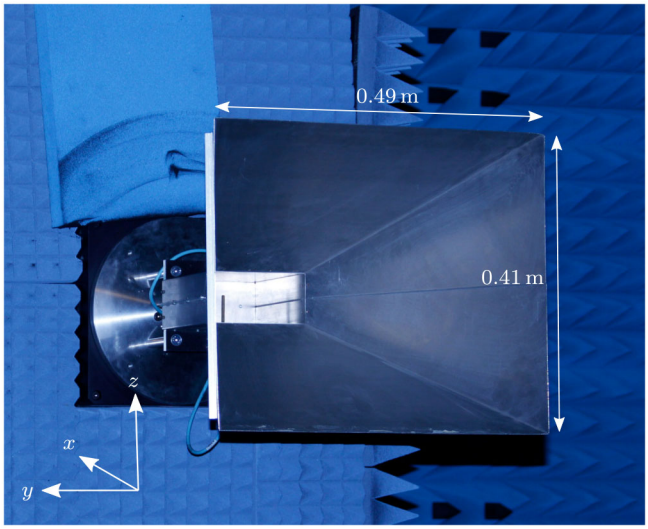

FIGURE 18. Photograph of the horn antenna installed to the positioner of the standard spherical roll-over-azimuth measurement system.

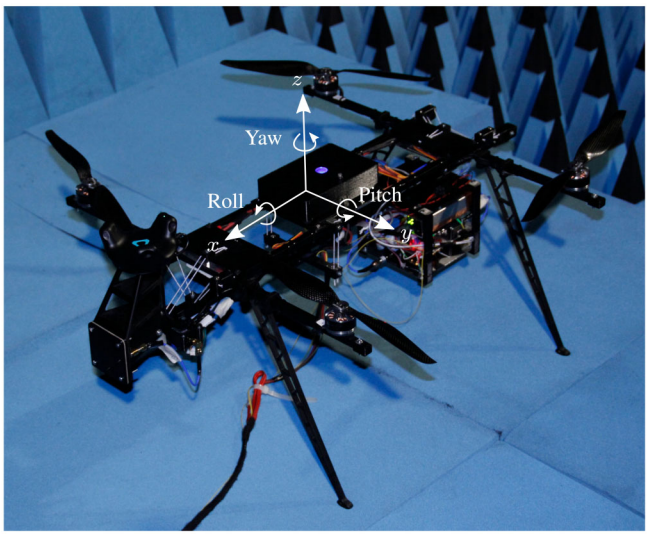

FIGURE 19. Photograph of the assembled quad-rotor measurement platform and definition of the body coordinate system.

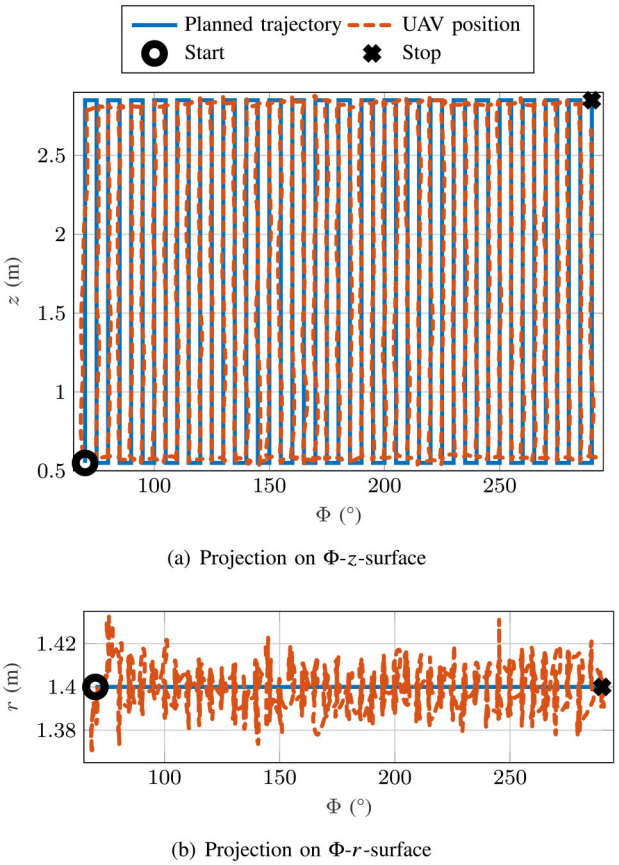

FIGURE 20. Projection of the planned trajectory and actual position of the UAV gravity center during the cylindrical near-field measurement (a) onto the Φ-z-surface and (b) onto the Φ-r-surface.

The trajectory for the gravity center of the UAV was generated under consideration of the spatial conditions in the measurement chamber, i.e., avoiding collisions of the UAV with the roll-over-azimuth positioner and with the absorbers at the chamber walls, floor, and ceiling. As a compromise, the cylinder is centered at (1.6 m, 0.0 m, 1.7 m) in the tracking coordinate system with a radius of 1.4 m and a height of 2.3 m. It covers an angular range of $80° \leq \Phi \leq 280°$. Due to the distance of 0.39 m between the UAV's gravity center and the probe antenna, the effective measurement radius is only about 1 m. Measurement samples below 0.65 m and above 2.75 m are discarded for the NFFFT to avoid over-weighting of the near-field observations at the top and bottom edges of the meander flight path. Considering that the cylinder axis is about half a meter in front of the AUT's aperture center, the valid angular range of the far-field results is $65° \leq \vartheta \leq 122°$ for the E-plane and $90° \leq \varphi \leq 270°$ for the H-plane.

A projection of the planned meander trajectory on the Φ-z-cylinder surface is shown in Fig. 20(a). The maximum acceleration and velocity of the motion profile are limited to 0.25 m/s^2 and 0.3 m/s, respectively. The vertical sections are separated by $\Delta\Phi = 5°$, i.e., an arc length of 12 cm. This results in a flight time of approximately 9 min for the trajectory on which the measurements are taken. Fig. 20(a) also shows the actual UAV flight path recorded for one of the measurements to illustrate the deviations in Φ- and $z-$direction from the planned trajectory. The flight path deviations in radial r-direction are given in Fig. 20(b). It can be seen that despite the disturbing force of the swinging cable connecting the UAV to the ground station and the air turbulances in the small chamber, the deviation of the UAV flight path from the planned trajectory is in the range of only a few centimeters. The probe antenna Euler orientation angles, as defined in Fig. 6, are plotted over the measurement time in Fig. 21.

Almost negligible deviations from the ideal angles ($\alpha = \Phi - 180°$, $\beta = \gamma = 0°$) along the cylindrical surface can be observed. Only the polarization angle γ has a small offset due to some misalignment between the upper and lower

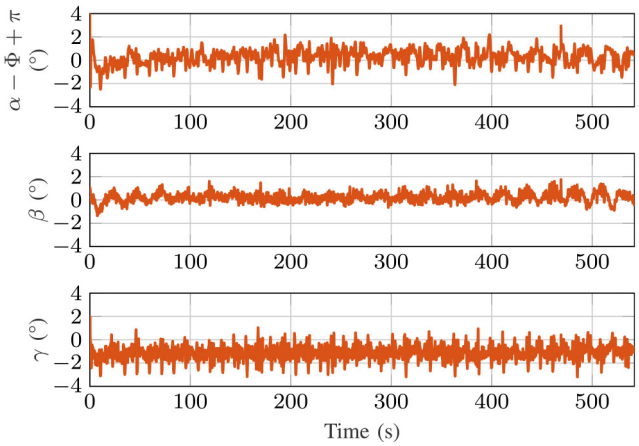

FIGURE 21. Euler orientation angles α, β and γ of the probe antenna as defined in Fig. 6 during the cylindrical scan of Fig. 20.

section of the drone frame. Of course, the flight dynamics demand a change of the orientation angles in order to follow the trajectory by steering the thrust vector. However, the mechanical decoupling of the frame sections dampens rapid changes and the probe orientation is anyway considered in the probe correction of the NFFFT.

The distance trigger for the RF signal sampling of both probe polarization was set to 5 mm. With an angular step size of $\Delta\Phi = 5°$, the near-field is over-sampled. In combination with the IESS, this helps to mitigate the effect of room scattering through spatial filtering. The equivalent sources are defined on a closed hull surface that is 5 cm larger than the actual horn in all dimensions.

For all measurements, the SDR's amplifiers are configured for a dynamic range of at least 50 dB with a safety margin to prevent SDR receiver overload.

The flight procedure of a planar measurement for the horn antenna in the anechoic chamber can be watched in the video that accompanies this contribution.

B. MEASUREMENT RESULTS FOR 1.8 GHZ

First, the near-field of the vertically polarized horn antenna was measured on the cylinder surface at 1.8 GHz with the corresponding dual-polarized probe antenna installed at the UAV's tracker-probe-antenna unit. The magnitude of the obtained signal for probe port 1 and 2 are shown in Fig. 22(a) and the signals' phase is given in Fig. 22(b).

In main beam direction, only a moderate magnitude drop towards the top and bottom of the cylindrical scan area can be observed. This inevitable leads to truncation errors in the far field, especially at the edges of the valid angular regions.

From the measured near-field samples, the IESS computes the equivalent electric and magnetic surface current densities. Fig. 23 visualizes the magnitude of the equivalent Love currents on the hull surface for the SNF reference scan and the UAV-based measurement. Slight differences between the results can mainly be attributed to the vertical scan area truncation.

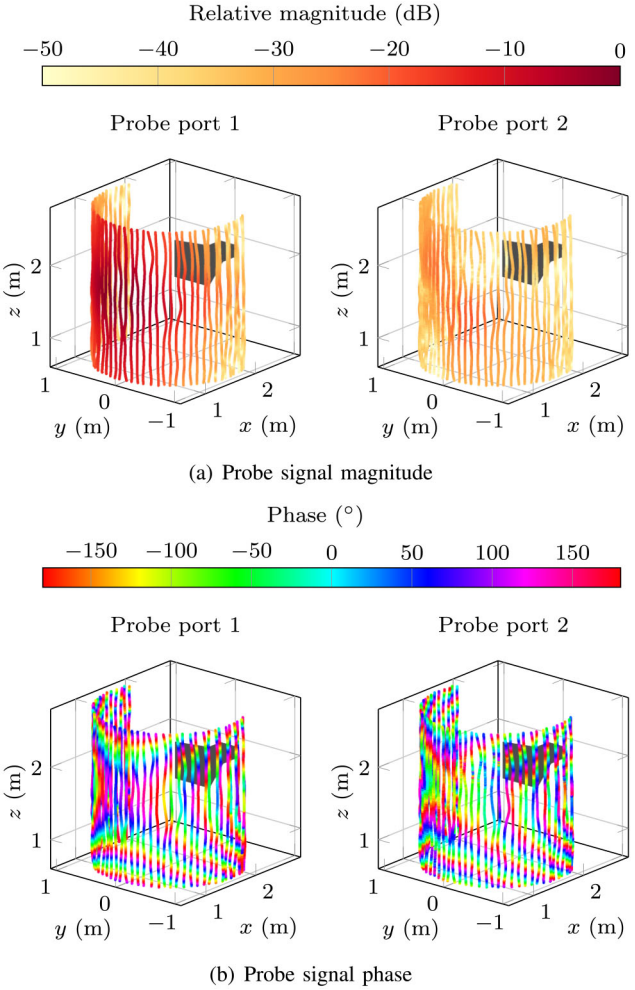

FIGURE 22. Probe port 1/2 signal (a) normalized magnitude and (b) phase for the UAV-based measurement at 1.8 GHz.

In the next step, the IESS computes the far-field of the equivalent sources in Fig. 23 to complete the NFFFT. The E- and H-plane far-field cuts for the reference and UAV-based measurement are shown in Fig. 24(a) and Fig. 24(b), respectively. Regions outside of the valid angular region of approximately ±30° around the E-plane center are marked in grey. For comparison, the relative far-field deviation

$$\varepsilon(\vartheta,\varphi) = 20\log\left(\left|\frac{|E^{\mathrm{UAV}}(\vartheta,\varphi)|}{E^{\mathrm{UAV}}_{\mathrm{max}}} - \frac{|E^{\mathrm{Ref}}(\vartheta,\varphi)|}{E^{\mathrm{Ref}}_{\mathrm{max}}}\right|\right) \quad (8)$$

is defined as the difference between the far-field magnitudes of the UAV-based result $E^{\mathrm{UAV}}(\vartheta,\varphi)$ and the reference $E^{\mathrm{Ref}}(\vartheta,\varphi)$. Both are normalized to the maximum magnitude $E^{\mathrm{UAV}}_{\mathrm{max}}$ and $E^{\mathrm{Ref}}_{\mathrm{max}}$, respectively, of the considered far-field cut. The maximum deviation for the co-polar field component E_ϑ is around −40 dB inside the valid region and increases outside due to the truncation error. The use of the simulated instead of a measured far-field pattern for probe correction is assumed to cause the higher maximum deviation for the cross polar component E_φ. This behavior is also visible for the H-plane, where, however, truncation errors are

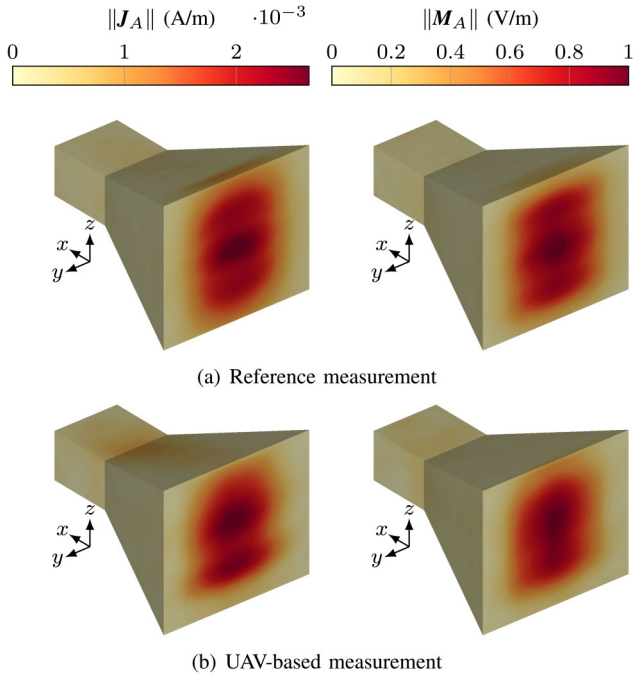

FIGURE 23. Normalized equivalent Love surface current densities on the hull surface enclosing the horn antenna obtained (a) from the standard SNF measurement and (b) from the cylindrical UAV-based near-field measurement at 1.8 GHz.

much smaller due to the stronger magnitude taper of the near-field towards the right and left edges of the cylindrical measurement surface.

C. REPEATABILITY CHECK AT 1.8 GHZ

The same measurement as in the previous section was repeated with the gain of the SDR amplifiers reduced by 4 dB to check the repeatability as well as the linearity of the measurement system. Fig. 25 shows the projection of the actual flight path on the cylinder surface for both measurements. Due to the varying impact of the swinging cable to the ground station and air turbulances on the flight trajectory, the near-field is measured at slightly different locations. The excellent agreement of the IESS far-field solutions for the measurements in Fig. 26 prove that the system delivers stable results. The remaining deviations are caused by measurement noise (the SDR's amplifier gain was reduced by 4 dB), room scattering and systematic errors of the tracking system that lead to slightly different probe position and orientation errors for the two non-identical flight paths.

D. MEASUREMENT RESULTS FOR 2.7 GHZ

For the measurements at 2.7 GHz, the dual-polarized probe patch antenna was exchanged and the SDR's LO frequency was changed accordingly. The gain of the SDR amplifiers were adjusted to retain a dynamic range of about 50 dB. Then, a measurement was performed on the same flight path as previously. Magnitude and phase of the near-field signals are shown in Fig. 27(a) and Fig. 27(b) for both probe antenna ports. At 2.7 GHz, higher modes are excited in the

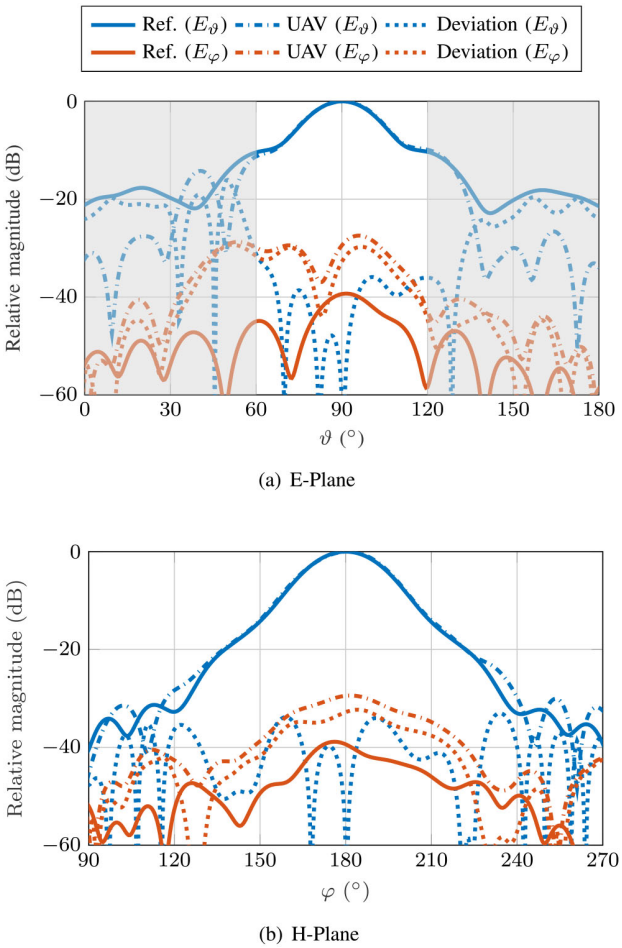

FIGURE 24. E-plane and H-Plane far-field result of the SNF reference and UAV-based measurement at 1.8 GHz. For the E-Plane, the region outside the valid angular range is marked in grey.

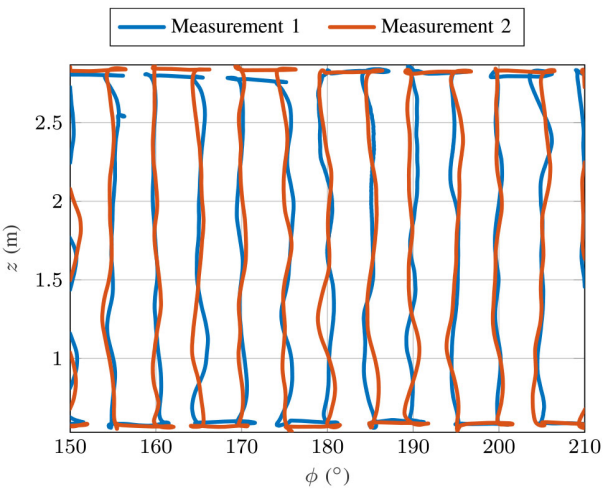

FIGURE 25. Projection of the UAV flight path during measurement 1 and 2 of the repeatability test onto the ϕ-z-surface. Only a section of the total path is shown to make differences more noticeable.

waveguide feed section with a width of 15 cm and a height of 7.5 cm. Compared to the measurements at 1.8 GHz, where just the fundamental mode is excited in the feed section, the

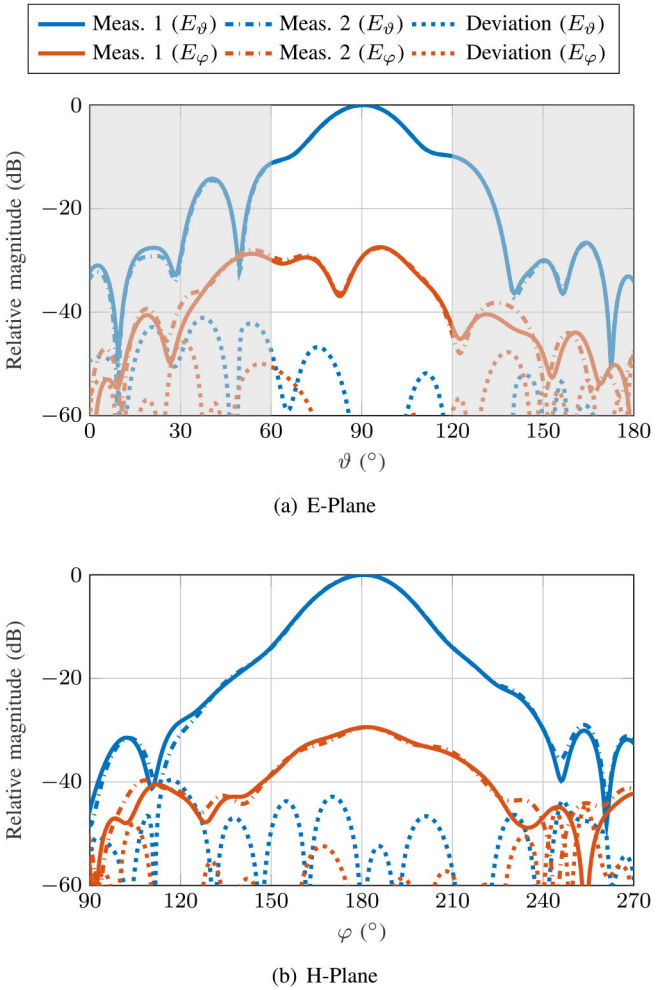

FIGURE 26. E-plane and H-Plane far-field results of the repeatability check at 1.8 GHz. For the E-Plane cut, the region outside the valid angular range is marked in grey.

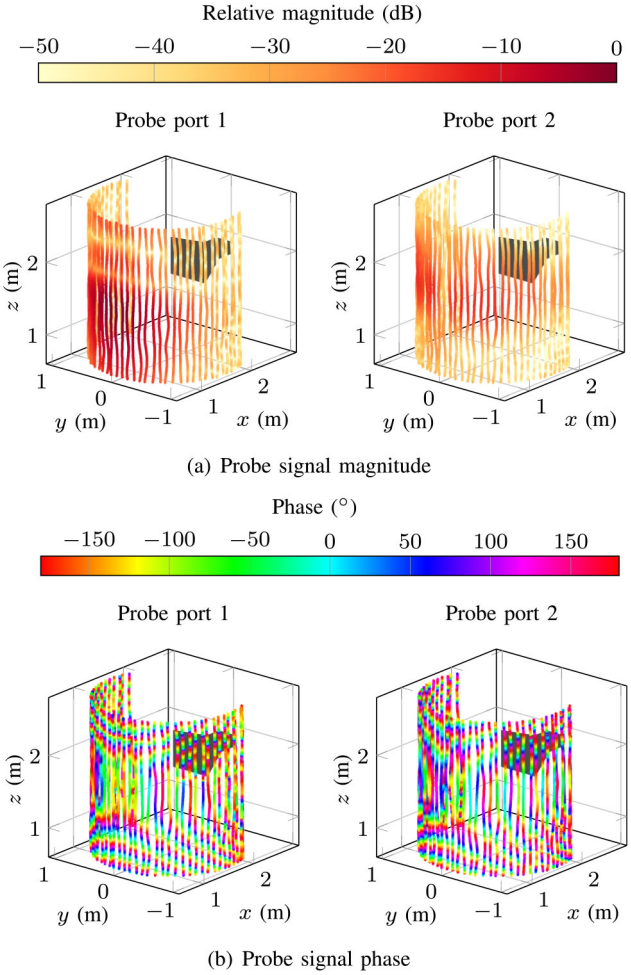

FIGURE 27. Probe port 1/2 signal (a) normalized magnitude and (b) phase for the UAV-based measurement at 2.7 GHz.

higher modes cause the horn to radiate more towards the bottom, as can be seen in the near-field magnitude plots.

The effect of the overmoded waveguide operation is also evident in the reconstructed surface current densities in Fig. 28. Compared to the typical horn aperture field distribution in Fig. 23, the field concentrates in the lower half of the aperture. Nevertheless, the stronger vertical near field magnitude taper, at least towards the top of the cylinder, reduces the truncation error and results in a better agreement of the currents from the UAV-based measurement with the SNF scan measurement.

As already indicated by the near-field distribution on the cylindrical surface, the E-plane far-field result in Fig. 29(a) shows a tilt of the main beam towards the ground. For that reason, the H-plane cut in Fig. 29(b) was evaluated at the beam peak at $\vartheta = 96°$. Again, the relative error of the co-polar component for the H-plane, which is less affected by truncation errors, is around -40 dB. For the cross-polar field component, the deviation is only slightly higher because, this time, the actually measured far-field pattern of the 2.7 GHz dual-polarized probe antenna was used for the probe correction.

V. CONCLUSION

It has been demonstrated that a UAV-based near-field antenna measurement system for frequencies up to several GHz can be built from very cost-effective components. With an appropriate scan strategy, the tethered UAV is a very flexible platform to maneuver the near-field probe around a stationary AUT. The customized "H"-shaped frame is superior to off-the-shelf UAVs with its optimized probe position that minimizes scattering from the UAV frame and rotor blades and simple re-balancing of the drone's gravity center by adjusting the position of the equipment carrier.

The dual-channel SDR LimeSDR turned out to be well-suited to measure and pre-process the signals of the dual-polarized probe antenna including filtering and decimation. Some measures were taken to reduce the crosstalk between the Tx and Rx channels. An additional calibration circuit was implemented for channel balancing and measurement of the thermal drift during the flight phase that is corrected in a post-processing step. The designed RFoF link proved to be a

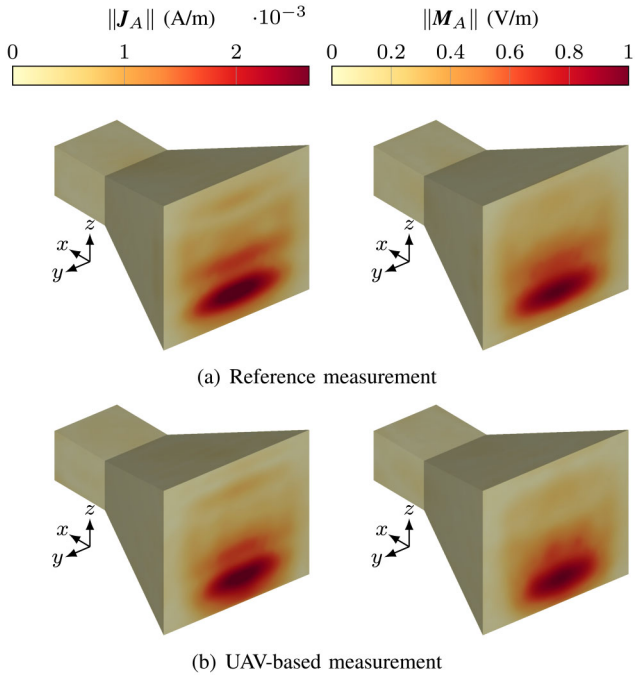

FIGURE 28. Normalized equivalent Love surface current densities on the hull surface enclosing the horn antenna obtained (a) from the standard SNF measurement and (b) from the cylindrical UAV-based near-field measurement at 2.7 GHz. The equivalent current distributions strongly differ from those in Fig. 23 because higher order waveguide modes are excited in the feed section of the horn.

good alternative to heavy, stiff and expensive coaxial cables. For phase-coherent near-field measurements, it transmits the constant power RF signal from the flying UAV to the AUT on the ground.

The low-cost 6-D Valve Index tracking system designed for VR applications reliably provides position and orientation information of the probe antenna with sufficient accuracy for the subsequent NFFFT at frequencies of several GHz. Nevertheless, a more sophisticated system calibration at multiple points in space is desirable to improve the tracking accuracy in the covered volume.

The developed operator software with a GUI allows convenient control of the UAV and the measurement process. It guides the UAV along a predefined flight path and records the probe antenna signals and pose data. The acquired UAV measurements unleash the full potential of IESSs such as the employed FIAFTA. It efficiently processes irregularly distributed measurement points as they inevitable occur for UAV-based measurement platforms. Moreover, the inherent probe correction feature of the MLFMM-based algorithm allows full correction of the influence of the arbitrarily oriented probe antenna.

The presented measurement results for the horn antenna demonstrated an excellent repeatability despite slightly different flight paths. For both frequencies, 1.8 GHz and 2.7 GHz, the comparison with the results of a conventional SNF scan revealed an accuracy of about −40 dB for the co-polar component of the far-field results in the H-plane cuts which are less affected by truncation errors due to the limited vertical extension of the cylindrical measurement surface.

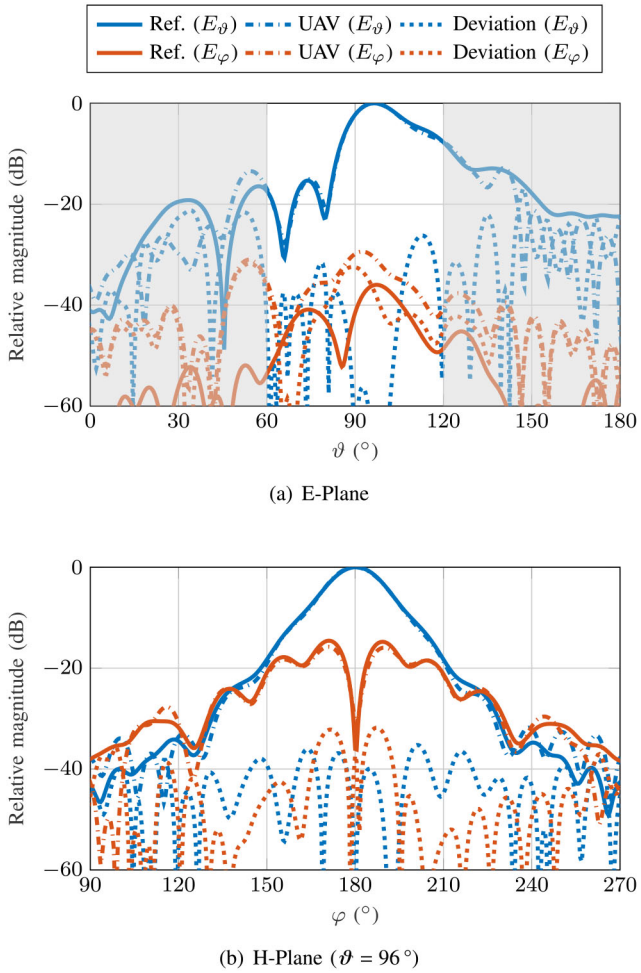

FIGURE 29. E-plane and H-Plane far-field result of the SNF reference and UAV-based measurement at 2.7 GHz. For the E-Plane, the region outside the valid angular range is marked in grey.

ACKNOWLEDGMENT

The authors would like to thank Torsten Fritzel from Aeroxess GmbH whose inspiration led to this work.

REFERENCES

[1] H. Shakhatreh *et al.*, "Unmanned aerial vehicles (UAVs): A survey on civil applications and key research challenges," *IEEE Access*, vol. 7, pp. 48572–48634, 2019.

[2] N. Chahat *et al.*, "The mars helicopter telecommunication link: Antennas, propagation, and link analysis," *IEEE Antennas Propag. Mag.*, vol. 62, no. 6, pp. 12–22, Dec. 2020.

[3] J. Schreiber, "Antenna pattern reconstitution using unmanned aerial vehicles (UAVs)," in *Proc. IEEE Conf. Antenna Meas. Appl. (CAMA)*, Oct. 2016, pp. 1–3.

[4] "Colibrex GMBH." Accessed: Jun. 19, 2022. [Online]. Available: https://www.colibrex.com/

[5] R. Geise *et al.*, "Nearfield inspection of navigation systems with UAVs—first results from the NAVANT project," in *Air Traffic Management and Systems IV*, E. N. R. Institute, Ed. Singapore: Springer, 2021, pp. 337–351, doi: 10.1007/978-981-33-4669-7_20.

[6] A. Salari and D. Erricolo, "Unmanned aerial vehicles for high-frequency measurements: An accurate, fast, and cost-effective technology," *IEEE Antennas Propag. Mag.*, vol. 64, no. 1, pp. 39–49, Feb. 2022.

[7] G. Virone *et al.*, "Preliminary results on the verification of the LOFAR-HBA with a flying test source," in *Proc. 15th Eur. Conf. Antennas and Propag. (EuCAP)*, 2021, pp. 1–4.
[8] G. Virone *et al.*, "Measurement of the LOFAR-HBA beam patterns using an unmanned aerial vehicle in the near field," *J. Astron. Telescopes Instrum. Syst.*, vol. 8, no. 1, pp. 1–14, 2021. [Online]. Available: https://doi.org/10.1117/1.JATIS.8.1.011005
[9] L. Ciorba *et al.*, "Large horizontal near-field scanner based on a non-tethered unmanned aerial vehicle," *IEEE Open J. Antennas Propag.*, vol. 3, pp. 568–582, 2022.
[10] A. Adhyapak, M. Diddi, M. Kling, A. Colby, and H. Singh, "Exploration of anechoic chamber characterization with autonomous unmanned aerial systems," in *Proc. 15th Eur. Conf. Antennas Propag. (EuCAP)*, 2021, pp. 1–5.
[11] J. A. Gordon *et al.*, "Millimeter-wave near-field measurements using coordinated robotics," *IEEE Trans. Antennas Propag.*, vol. 63, no. 12, pp. 5351–5362, Dec. 2015.
[12] J. Hatzis, P. Pelland, and G. Hindman, "Implementation of a combination planar and spherical near-field antenna measurement system using an industrial 6-axis robot," in *Proc. 38th Annu. Symp. Antenna Meas. Techn. Assoc. (AMTA)*, Austin, TX, USA, Oct. 2016, pp. 1–6.
[13] A. Geise *et al.*, "A crane-based portable antenna measurement system—System description and validation," *IEEE Trans. Antennas Propag.*, vol. 67, no. 5, pp. 3346–3357, May 2019.
[14] G. Álvarez-Narciandi, J. Laviada, Y. Álvarez-López, and F. Las-Heras, "Portable freehand system for real-time antenna diagnosis and characterization," *IEEE Trans. Antennas Propag.*, vol. 68, no. 7, pp. 5636–5645, Jul. 2020.
[15] F. T. Faul, H.-J. Steiner, and T. F. Eibert, "Near-field antenna measurements with manual collection of the measurement samples," *Adv. Radio Sci.*, vol. 18, pp. 17–22, Dec. 2020. [Online]. Available: https://ars.copernicus.org/articles/18/17/2020/
[16] T. Fritzel, H. Steiner, J. Hartmann, and J. Habersack, "Revolutionary new outdoor testing with a mobile airborne nearfield test facility (ANTF)," in *Proc. 24th Annu. Symp. Antenna Meas. Techn. Assoc. (AMTA)*, Cleveland, OH, USA, Nov. 2002, pp. 1–6.
[17] P. Henkel, A. Sperl, U. Mittmann, T. Fritzel, R. Strauss, and H. Steiner, "Precise 6D RTK positioning system for UAV-based near-field antenna measurements," in *Proc. 14th Eur. Conf. Antennas Propag. (EuCAP)*, 2020, pp. 1–5.
[18] F. Paonessa *et al.*, "Recent results in antenna pattern measurement with UAVs," in *Proc. Int. Conf. Electromagn. Adv. Appl. (ICEAA)*, Sep. 2015, pp. 720–721.
[19] F. Paonessa *et al.*, "Effect of the UAV orientation in antenna pattern measurements," in *Proc. 9th Eur. Conf. Antennas Propag. (EuCAP)*, Apr. 2015, pp. 1–2.
[20] G. Virone *et al.*, "UAV-based antenna and field measurements," in *Proc. IEEE Conf. Antenna Meas. Appl. (CAMA)*, Oct. 2016, pp. 1–3.
[21] F. Paonessa *et al.*, "VHF/UHF antenna pattern measurement with unmanned aerial vehicles," in *Proc. IEEE Metrol. Aerosp. (MetroAeroSpace)*, Jun. 2016, pp. 87–91.
[22] G. Virone *et al.*, "Antenna pattern measurement with UAVs: Modeling of the test source," in *Proc. 10th Eur. Conf. Antennas Propag. (EuCAP)*, Apr. 2016, pp. 1–3.
[23] F. Paonessa, G. Virone, P. Bolli, and A. M. Lingua, "UAV-based antenna measurements: Scan strategies," in *Proc. 11th Eur. Conf. Antennas Propag. (EUCAP)*, Mar. 2017, pp. 1303–1305.
[24] L. Ciorba *et al.*, "Near-field phase reconstruction for UAV-based antenna measurements," in *Proc. 13th Eur. Conf. Antennas Propag. (EuCAP)*, Mar. 2019, pp. 1–4.
[25] J. Zhang *et al.*, "Beam measurements of the Tianlai dish radio telescope using an unmanned aerial vehicle [antenna applications corner]," *IEEE Antennas Propag. Mag.*, vol. 63, no. 6, pp. 98–109, Dec. 2021.
[26] M. García-Fernández *et al.*, "Antenna diagnostics and characterization using unmanned aerial vehicles," *IEEE Access*, vol. 5, pp. 23563–23575, 2017.
[27] M. Garcia-Fernandez, Y. Alvarez-Lopez, and F. Las-Heras, "UAV-based antenna measurement and diagnostics for circularly polarized antenna arrays," in *Proc. IEEE Int. Symp. Antennas Propag. USNC/URSI Nat. Radio Sci. Meeting*, Jul. 2018, pp. 525–526.
[28] M. G. Fernández, Y. Álvarez López, and F. L. Andrés, "Advances in antenna measurement and characterization using unmanned aerial vehicles," in *Proc. 13th Eur. Conf. Antennas Propag. (EuCAP)*, Mar. 2019, pp. 1–5.
[29] M. G. Fernández, Y. Á. López, and F. L. Andrés, "Antenna measurement and diagnostics processing techniques using unmanned aerial vehicles," in *Proc. 13th Eur. Conf. Antennas Propag. (EuCAP)*, Mar. 2019, pp. 1–5.
[30] "OptiTrack." NaturalPoint. Accessed: Jun. 19, 2022. [Online]. Available: https://optitrack.com/
[31] "Laser Tracker Systems." Leica Geosystems AG. Accessed: Jun. 19, 2022. [Online]. Available: https://leica-geosystems.com/en-us/products/laser-tracker-systems
[32] T. Fritzel, R. Strauß, H. Steiner, C. Eisner, and T. Eibert, "Introduction into an UAV-based near-field system for in-situ and large-scale antenna measurements (invited paper)," in *Proc. IEEE Conf. Antenna Meas. Appl. (CAMA)*, Oct. 2016.
[33] T. Fritzel, H. Steiner, and R. Strauß, "Laser tracker metrology for UAV-based antenna measurements," in *Proc. IEEE Conf. Antenna Meas. Appl. (CAMA)*, Sep. 2018, pp. 1–3.
[34] G. Virone *et al.*, "Antenna pattern verification system based on a micro unmanned aerial vehicle (UAV)," *IEEE Antennas Wireless Propag. Lett.*, vol. 13, pp. 169–172, 2014.
[35] F. T. Faul and T. F. Eibert, "Setup and error analysis of a fully coherent UAV-based near-field measurement system," in *Proc. 15th Eur. Conf. Antennas Propag. (EuCAP)*, 2021, pp. 1–4.
[36] "Active Target." Automated Precision. Accessed: Jun. 19, 2022. [Online]. Available: https://apimetrology.com/active-target/
[37] S. Punzet *et al.*, "Fully coherent UAV-based near-field measurement and transformation of the S67-15m ground station antenna at the German space operations center in Weilheim," in *Proc. 16th Eur. Conf. Antennas Propag. (EuCAP)*, 2022, pp. 1–5.
[38] Y. Alvarez, F. Las-Heras, and M. R. Pino, "Reconstruction of equivalent currents distribution over arbitrary three-dimensional surfaces based on integral equation algorithms," *IEEE Trans. Antennas Propag.*, vol. 55, no. 12, pp. 3460–3468, Dec. 2007.
[39] J. L. A. Quijano and G. Vecchi, "Field and source equivalence in source reconstruction on 3D surfaces," *Progr. Electromagn. Res.*, vol. 103, pp. 67–100, Apr. 2010.
[40] T. F. Eibert and C. H. Schmidt, "Multilevel fast multipole accelerated inverse equivalent current method employing Rao–Wilton–Glisson discretization of electric and magnetic surface currents," *IEEE Trans. Antennas Propag.*, vol. 57, no. 4, pp. 1178–1185, Apr. 2009.
[41] T. F. Eibert, E. Kilic, C. Lopez, R. A. M. Mauermayer, O. Neitz, and G. Schnattinger, "Electromagnetic field transformations for measurements and simulations," *Progr. Electromagn. Res.*, vol. 151, pp. 127–150, May 2015.
[42] O. Neitz, R. A. M. Mauermayer, Y. Weitsch, and T. F. Eibert, "A propagating plane-wave-based near-field transmission equation for antenna gain determination from irregular measurement samples," *IEEE Trans. Antennas Propag.*, vol. 65, no. 8, pp. 4230–4238, Aug. 2017.
[43] J. Kornprobst, R. A. Mauermayer, O. Neitz, J. Knapp, and T. F. Eibert, "On the solution of inverse equivalent surface-source problems," *Progr. Electromagn. Res.*, vol. 165, pp. 47–65, Aug. 2019.
[44] J. Kornprobst, J. Knapp, R. A. M. Mauermayer, O. Neitz, A. Paulus, and T. F. Eibert, "Accuracy and conditioning of surface-source based near-field to far-field transformations," *IEEE Trans. Antennas Propag.*, vol. 69, no. 8, pp. 4894–4908, Aug. 2021.
[45] C. Parini, J. McCormick, S. Gregson, T. Eibert, and D. van Rensburg, *Theory and Practice of Modern Antenna Range Measurements*. London, U.K.: Inst. Eng. Technol., 2020.
[46] T. F. Eibert and J. Migl, "Inverse surface-source solutions for very large antennas—The one thousand wavelength aperture," in *Proc. 15th Eur. Conf. Antennas Propag. (EuCAP)*, 2021, pp. 1–4.
[47] O. Borries *et al.*, "A fast source reconstruction method for radiating structures on large scattering platforms," in *Proc. 43rd Annu. Symp. Antenna Meas. Techn. Assoc. (AMTA)*, 2021, pp. 1–6.
[48] A. Paulus, J. Knapp, and T. F. Eibert, "Phaseless near-field far-field transformation utilizing combinations of probe signals," *IEEE Trans. Antennas Propag.*, vol. 65, no. 10, pp. 5492–5502, Oct. 2017.
[49] J. Kornprobst, A. Paulus, J. Knapp, and T. F. Eibert, "Phase retrieval for partially coherent observations," *IEEE Trans. Signal Process.*, vol. 69, pp. 1394–1406, Feb. 2021.
[50] R. A. M. Mauermayer, J. Kornprobst, and T. Fritzel, "A low-cost multicopter based near-field antenna measurement system employing software defined radio and 6-D laser metrology," in *Proc. 41st Annu. Symp. Antenna Meas. Techn. Assoc. (AMTA)*, San Diego, CA, USA, Oct. 2019, pp. 1–5.

[51] J. Kornprobst, R. A. M. Mauermayer, and T. F. Eibert, "Versatile low-cost and light-weight RF equipment for field measurements," in *Proc. 14th Eur. Conf. Antennas Propag. (EuCAP)*, Mar. 2020, pp. 1–3.
[52] "Valve Corporation." Accessed: Jun. 19, 2022. [Online]. Available: https://www.valvesoftware.com
[53] "Vive Tracker." HTC Corporation. Accessed: Jun. 19, 2022. [Online]. Available: https://www.vive.com/us/accessory/vive-tracker/
[54] T. Fritzel, H. Steiner, and R. Strauß, "Advances in the development of an industrial UAV for large-scale near-field antenna measurements," in *Proc. 13th Eur. Conf. Antennas Propag. (EuCAP)*, Mar. 2019, pp. 1–3.
[55] A. Y. Umeyama, J. L. Salazar-Cerreno, and C. J. Fulton, "UAV-based antenna measurements for polarimetric weather radars: Probe analysis," *IEEE Access*, vol. 8, pp. 191862–191874, 2020.
[56] G. Virone *et al.*, "Effect of conductive propellers on VHF UAV-based antenna measurements: Simulated results," in *Proc. 15th Eur. Conf. Antennas Propag. (EuCAP)*, 2021, pp. 1–4.
[57] F. T. Faul, D. Korthauer, and T. F. Eibert, "Impact of rotor blade rotation of UAVs on electromagnetic field measurements," *IEEE Trans. Instrum. Meas.*, vol. 70, pp. 1–9, Sep. 2021.
[58] D. C. Niehorster, L. Li, and M. Lappe, "The accuracy and precision of position and orientation tracking in the HTC vive virtual reality system for scientific research," *i-Perception*, vol. 8, no. 3, Jun. 2017, Art. no. 2041669517708205.
[59] P. Hyatt, D. Kraus, V. Sherrod, L. Rupert, N. Day, and M. D. Killpack, "Configuration estimation for accurate position control of large-scale soft robots," *IEEE/ASME Trans. Mechatronics*, vol. 24, no. 1, pp. 88–99, Feb. 2019.
[60] M. Borges, A. C. Symington, B. Coltin, T. Smith, and R. Ventura, "HTC Vive: Analysis and accuracy improvement," in *Proc. IEEE/RSJ Int. Conf. on Intell. Robots Syst. (IROS)*, 2018, pp. 2610–2615.
[61] J. Lwowski, A. Majumdat, P. Benavidez, J. J. Prevost, and M. Jamshidi, "HTC Vive tracker: Accuracy for indoor localization," *IEEE Syst., Man, Cybern., Mag.*, vol. 6, no. 4, pp. 15–22, Oct. 2020.
[62] "Open Source Lighthouse Tracking System." Accessed: Jun. 19, 2022. [Online]. Available: https://github.com/cntools/libsurvive
[63] R. Hartley and A. Zisserman, *Multiple View Geometry in Computer Vision*. Cambridge, U.K.: Cambridge Univ. Press, 2003.
[64] P. Bauer, W. Lienhart, and S. Jost, "Accuracy investigation of the pose determination of a VR system," *Sensors*, vol. 21, no. 5, p. 1622, 2021. [Online]. Available: https://www.mdpi.com/1424-8220/21/5/1622
[65] L. Meier. "PX4 Autopilot." Accessed: Jun. 19, 2022. [Online]. Available: https://px4.io/
[66] L. Meier. "Pixhawk." Accessed: Jun. 19, 2022. [Online]. Available: http://pixhawk.org/
[67] "Raspberry Pi 3 Model B." Raspberry Pi Foundation. Accessed: Jun. 19, 2022. [Online]. Available: https://www.raspberrypi.org/products/raspberry-pi-3-model-b/
[68] "MAVProxy." ArduPilot. Accessed: Jun. 19, 2022. [Online]. Available: https://ardupilot.org/mavproxy/index.html
[69] "MAVLink." Accessed: Jun. 19, 2022. [Online]. Available: https://mavlink.io/en/
[70] "USB/IP." Accessed: Jun. 19, 2022. [Online]. Available: http://usbip.sourceforge.net/
[71] "SteamVR." Accessed: Jun. 19, 2022. [Online]. Available: https://www.steamvr.com/
[72] "Qt." The Qt Company. Accessed: Jun. 19, 2022. [Online]. Available: https://www.qt.io/
[73] "OpenVR SDK." Valve Corporation. Accessed: Jun. 19, 2022. [Online]. Available: https://github.com/ValveSoftware/openvr
[74] "Lime Suite." Lime Microsystems. Accessed: Jun. 19, 2022. [Online]. Available: https://github.com/myriadrf/LimeSuite
[75] "CST Studio Suite." Dassault Systèmes. Accessed: Jun. 19, 2022. [Online]. Available: https://www.3ds.com/products-services/simulia/products/cst-studio-suite/
[76] R. Tena Sánchez and M. S. Castañer, "Evaluation of software defined radio receiver for phaseless near-field measurements," in *Proc. 40th Annu. Symp. Antenna Meas. Techn. Assoc. (AMTA)*, Williamsburg, VA, USA, Nov. 2018, pp. 1–6.
[77] R. T. Sanchez, M. S. Castaner, and L. J. Foged, "A referenceless antenna measurement system based on software-defined radio [measurements corner]," *IEEE Antennas Propag. Mag.*, vol. 62, no. 5, pp. 108–118, Oct. 2020.
[78] "LimeSDR." Lime Microsystems. Accessed: Jun. 19, 2022. [Online]. Available: https://myriadrf.org/projects/component/limesdr/
[79] "LMS7002M: FPRF MIMO Transceiver IC With Integrated Microcontroller." Lime Microsystems. Accessed: Jun. 19, 2022. [Online]. Available: https://limemicro.com
[80] "10G laserdiodes and photodiodes." Shenzhen YiGuDian Technology. Accessed: Aug. 20, 2022. [Online]. Available: http://gtellaser.en.trade-global.com/
[81] "iC-WKM: M-Type CW Laser Diode Driver." iC-Haus GmbH. Accessed: Jun. 19, 2022. [Online]. Available: https://www.ichaus.de
[82] (Analog Devices, Inc., Norwood, MA, USA). *HMC435A*. Accessed: Jun. 19, 2022. [Online]. Available: https://www.analog.com
[83] K. Shoemake, "Animating rotation with quaternion curves," in *Proc. 12th Annu. Conf. Comput. Graph. Interact. Techn.*, 1985, pp. 245–254.
[84] W. C. Chew, *Fast and Efficient Algorithms in Computational Electromagnetics* (Antennas and Propagation Library). Boston, MA, USA: Artech House, 2001.
[85] C. H. Schmidt, M. M. Leibfritz, and T. F. Eibert, "Fully probe-corrected near-field far-field transformation employing plane wave expansion and diagonal translation operators," *IEEE Trans. Antennas Propag.*, vol. 56, no. 3, pp. 737–746, Mar. 2008.
[86] S. M. Rao, D. Wilton, and A. W. Glisson, "Electromagnetic scattering by surfaces of arbitrary shape," *IEEE Trans. Antennas Propag.*, vol. 30, no. 3, pp. 409–418, May 1982.
[87] Y. Saad, *Iterative Methods for Sparse Linear Systems*. Boston, MA, USA: PWS, 1996.
[88] J. Kornprobst, O. Neitz, J. Knapp, R. A. M. Mauermayer, and T. F. Eibert, "Solving inverse equivalent surface source problems by the normal error system of normal equations," in *Proc. Int. Conf. Electromagn. Adv. Appl. (ICEAA)*, Sep. 2019, p. 989.
[89] J. Kornprobst, R. A. M. Mauermayer, E. Kiliç, and T. F. Eibert, "An inverse equivalent surface current solver with zero-field enforcement by left-hand side Calderón projection," in *Proc. 13th Eur. Conf. Antennas Propag. (EUCAP)*, Mar. 2019, pp. 1–3.

RAIMUND A. M. MAUERMAYER (Member, IEEE) received the Dipl.-Ing. degree in electrical engineering and information technology from the Technical University of Munich, Munich, Germany, in 2012.

From 2012 to 2018, he was a Research Assistant with the Chair of High-Frequency Engineering, Department of Electrical and Computer Engineering, Technical University of Munich. In 2019, he has joined the Research and Development department for Antenna Design and Measurement with Mercedes-Benz AG, Sindelfingen, Germany. His research interests include near-field to far-field transformations, field synthesis, and antenna measurement techniques.

JONAS KORNPROBST (Graduate Student Member, IEEE) received the B.Eng. degree in electrical engineering and information technology from the University of Applied Sciences Rosenheim, Rosenheim, Germany, in 2014, and the M.Sc. degree in electrical engineering and information technology from the Technical University of Munich, Munich, Germany, in 2016.

From 2016 to 2019, he was a Research Assistant with the Chair of High-Frequency Engineering, Department of Electrical and Computer Engineering, Technical University of Munich. In 2020, he has joined the Electronics Research and Development Department with Dr. Johannes Heidenhain GmbH, Traunreut, Germany. His current research interests include numerical electromagnetics, antenna measurement techniques and design, and virtual EMC testing.